Project No. 11-3195

Fundamental Studies of the Role of Grain Boundaries on Uniform Corrosion of Advanced Nuclear Reactor Materials

Nuclear Energy Advanced Modeling and Simulation (NEAMS)

Mitra Taheri
Drexel University

In collaboration with:
Pennsylvania State University
University of Michigan

Sue Lesica, Federal POC
Xin Sun, Technical POC

FINAL REPORT

Project Title: Fundamental Studies of the Role of Grain Boundaries on Uniform Corrosion of Advanced Nuclear Reactor Materials

Covering Period:	Final Report
Date of Report:	February 29, 2016
Recipient:	Drexel University 3141 Chestnut Street Philadelphia, PA 19104
Award Number:	11-3195
Principal Investigator:	Mitra Taheri, 215-895-6618, mtaheri@coe.drexel.edu
Co-PIs:	Arthur Motta, 814-865-0036, atm2@psu.edu Emmanuelle Marquis, 734-764-8717, emarq@umich.edu

Objective: The main objective of this proposal is to develop fundamental understanding of the role of grain boundaries in stable oxide growth. To understand the process of oxide layer destabilization, it is necessary to observe the early stages of corrosion. During conventional studies in which a sample is exposed and examined after removal from the autoclave, the destabilization process will normally have already taken place, and is only examined post facto. To capture the instants of oxide destabilization, it is necessary to observe it in-situ; however significant question always arise as to the influence of the corrosion geometry and conditions on the corrosion process. Thus *a combination of post facto examinations and in-situ studies is proposed, which also combines state-of-the-art characterization techniques to derive a complete understanding of the destabilization process and the role of grain boundaries*.

Background: The proposed Generation IV advanced nuclear systems and the higher duties demanded of existing light water reactors are creating harsher environments for materials than ever before and in many cases corrosion is the limiting design factor for the selection and implementation of materials. In the case of Generation IV reactors high temperatures and corrosive environments cause uniform corrosion to be a major challenge for the materials to be used in the reactor cores and balance of plant (DOE-NERAC, 2002). The corrosion rate depends strongly on the environment (temperature, pressure, chemistry), but, importantly, the corrosion rate also depends strongly on the alloy composition and microstructure. High temperature corrosion tests of various alloys are currently being conducted in the environments of relevance to these reactor concepts (Allen and Crawford 2003; Allen 2004). In particular ferritic-martensitic alloys such as HCM12A and NF616, as well as the older HT-9 and T91 alloys exhibit good resistance to swelling and cracking, but are susceptible to high temperature corrosion (DOE-NERAC, 2002). For existing light water-reactors (LWR), driven by the need to minimize waste volume, increase capacity factors and reduce fuel costs, the industry has been increasing average discharge fuel burnup and as a consequence residence time (Yang, 2000). Considerably less knowledge exists of fuel degradation mechanisms during these longer exposures. In addition to increased radiation damage increased amounts of corrosion and hydriding of the fuel are likely to occur. In addition, the primary water chemistry is more aggressive because of the chemical additions to the coolant necessary to operate at higher burnup. Finally, many reactors have received licenses for power uprates, which increases the outlet temperature and the incidence of boiling in the core of PWRs. Thus, the fuel is running at higher temperature and under more aggressive chemistry. All of these factors represent significantly increased fuel cladding duty. Alloys that resist corrosion do so by virtue of their development of a protective oxide layer that limits the access of corrosion species to the underlying metal, leading to stable oxide growth. The differences between a protective and a non-protective oxide lie in the oxide structure, which for a given environment, is determined by the alloy chemistry and microstructure. Very small changes in alloy microstructure can cause significant differences in corrosion rate. Thus, to design corrosion resistant alloys from a fundamental perspective, we need to understand the mechanisms of formation of a protective oxide and their relationship to the alloy microstructure.

1. Summary.

Work scope:
Work at Drexel University for focused on developing an *in-situ* TEM technique to study the initial corrosion behavior of common alloys for nuclear fuel rod cladding. This *in-situ* technique would be compared to ex-situ autoclave corroded samples provided by Pennsylvania State University. Following this, the effect of grain

boundaries and other microstructural features on the initial oxidation behavior of these alloys is to be studied. Samples tested using this technique were Zircaloy-4 and pure zirconium.

1. Site Specific *In Situ* TEM

To understand the role of interfacial structure in the corrosion, we have begun investigating methods for analyzing specific interfaces using in situ TEM. These experiments are outlined below.

2.1 Development of *In Situ* Stage

Preliminary design and testing was done to develop an in situ stage that will accommodate the experiments that we proposed for to achieve the goals outlined in our research. The progress of the implementation of such instrumentation is outlined below.

2.1.1. Initial Testing of E-Chip Design and Feasibility

The stage was designed PI Taheri in conjunction with Protochips (Raleigh, NC), and a three-phase plan was outlined.

2.1.2. Design of Drexel *In Situ* Holder

Per the 3-phased development plan outlined in the previous quarterly reports, Phase 1 has been completed. To review, details of the phase 1 holder are listed below.

Phase 1:

- Single tilt holder with 2 electrical contacts
- Tank---based manifold for non---flow pressure control
- Bubbler to introduce water saturated air
- Protochips Aduro III controller (both software and electrical control unit)
- Window and Heater E-chip devices

Implementation of Phase 1 has been completed (as of January 2013), and construction of the in situ TEM holder has begun. The "bubbler" design has been replaced with an atomizing nozzle design from a separate carrier line. This line will maintain its own flow, while the gas lines will enter the holder's viewing/reaction cell area in a different location, which maintains integrity of the carrier line materials. Ni-based alloys and low-carbon stainless steels were used after careful analysis of corrosion potential. Additionally, the cell will be capable of holding atmospheric pressure, based on the new design. After the holder was delivered and tested at Drexel, it was determined that a zeolite or similar material would be added to the bubbler line to be able to monitor relative humidity going into the holder from the bubbler.

Phase 2 and Beyond/Future Expectations for Development: Initially, for phase two, it was planned to upgrade to a full MFC--based gas manifold, as we do not have mass flow control on the current system. However, based on experience with other stages similar to the environmental cell, and based on our experience, it was decided that an MFC-based system would add huge complexity, with little gain in system versatility. Instead, an upgrade to the holder that allows for EDS compatibility was selected, which utilizes a change in top plate materials and design to allow for EDS during in-situ experiments. Also, in concurrent development is a new chip design for the environmental holder that will allow for the biasing of electronic devices and materials in severe environments.

Stage development and finalization: Work is starting for quantification of the humidity in the environmental cell in preparation for running oxidation experiments in humid environments. The material selected for these initial studies is soot, as soot collects and forms chains of small particles that when exposed to high humidity environments collapse and densify. In addition, humidity sensitive salts, including sodium chloride, potassium sulfate and potassium chloride, have been selected to use for use in humidity testing based on literature. Sample preparation methods are being developed, and initial characterization is underway. Working with Protochips, the current environmental TEM holder will be updated, with changes made to the top plate of the holder for EDS compatibility, in addition, the number of leads into the holder will be changed from two to four for better temperature control in conjunction with the new controller software. In addition, the increased number of leads will allow for additional options for biasing of devices under atmospheric conditions.

2.2 Characterization of Candidate Materials for In Situ TEM

2.2.1 Characterization of Zircaloy-4:

Work on this project started with the characterization of the as received oxidized Zircaloy-4 material. Bright field TEM, along with dark field and selected area diffraction were used, as shown in figure 1. This initial characterization was done using focused ion beam prepared samples from bulk material. These images will be used to compare corrosion at specific grain boundaries and in small areas of microstructures in as-received Zircaloy-4 sent to Drexel by co-PI Motta.

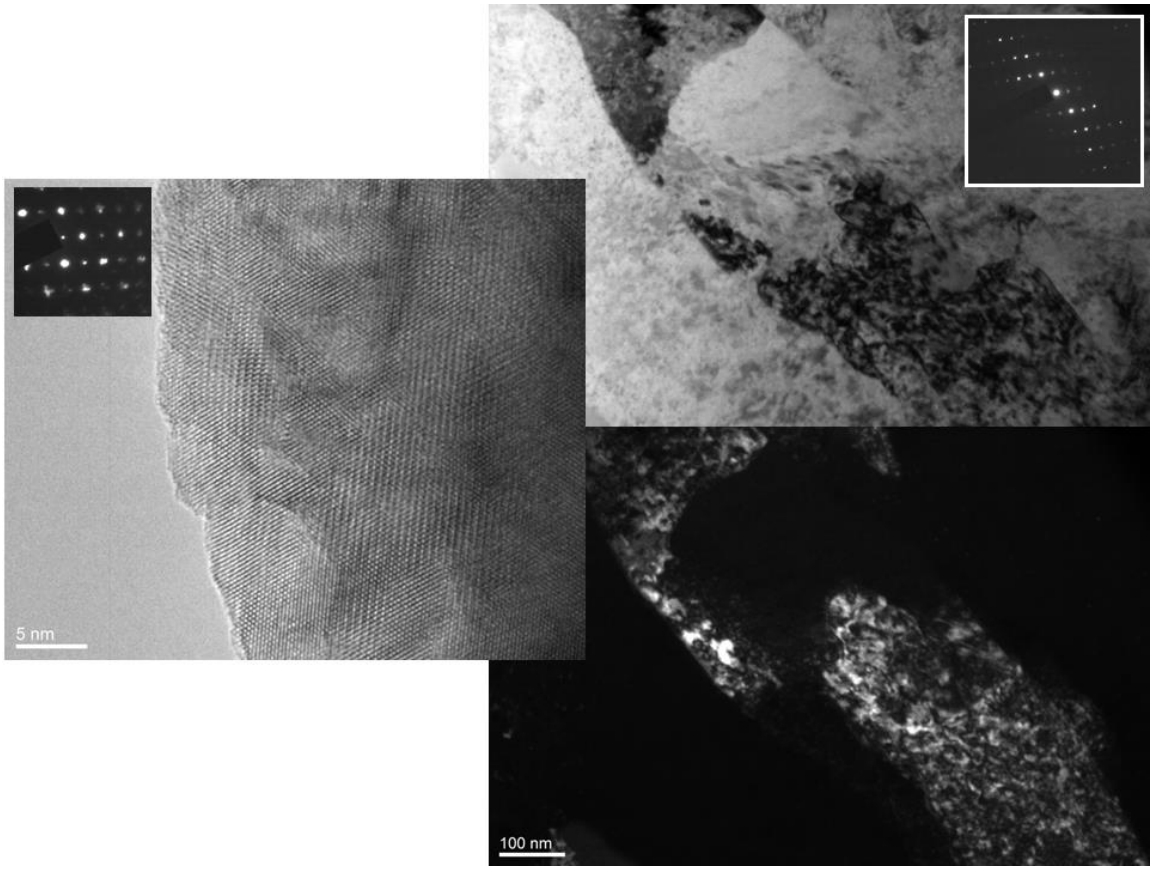

Figure 1: TEM brightfield/darkfield pairs (with corresponding diffraction), and high-resolution image (with corresponding diffraction) of oxide layers in as-corroded Zircaloy-4.

Initial characterization of the non-oxidized Zircaloy-4 was conducted on electropolished samples from bulk to give the best picture of the as received material with multiple microstructural features present in each sample. The electrolyte for this polish was 10% perchloric acid in methanol, chilled to -38°C.

2.2.2 Development of *In-situ* TEM sample preparation technique:

Following initial characterization, development of site-specific FIB preparation suitable for compatibility with the environmental cell holder E-chips was started. This process took longer than expected, as conventional methods of sample preparation using in-situ manipulation techniques proved to be unsuccessful. A variety of geometries

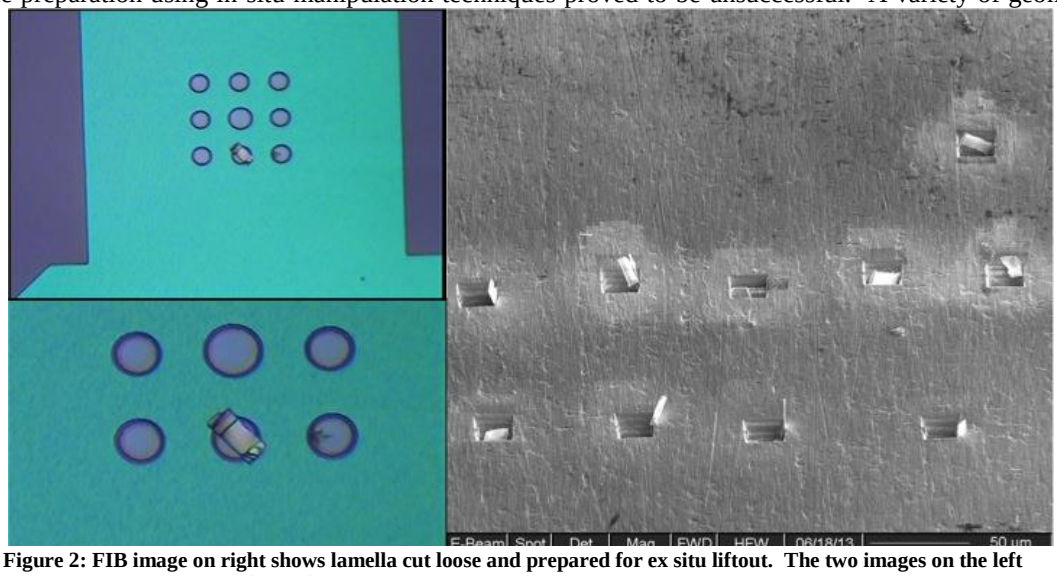

Figure 2: FIB image on right shows lamella cut loose and prepared for ex situ liftout. The two images on the left show a FIB sample successfully lifted out and placed over an electron transparent window on the E-chip

were tried for placing the sample on the E-chip sample support. After many unsuccessful attempts, it was concluded that in-situ manipulation of the FIB sample to the E-chip was not suitable, as it could not be performed reliably without breaking the E-chip membrane or losing the FIB sample when it broke loose from the omniprobe. At this point, other options were being explored for sample positioning. In figure 2, many FIB samples that have been prepared for lift out can be seen, along with the unique behavior that results when cutting the samples free in the trench. These samples were prepared to test the idea of using ex-situ lift out to place samples on the E-chip. Out of these lift-outs, three were successfully transferred to E-chips using an ex situ lift-out tool by an operator unfamiliar with working with E-chips. Unfortunately, two of these samples were lost since they were not attached to the chips using electron beam deposition in the FIB. This learning experience meant that all future samples prepared using ex situ lift-out will be placed in the FIB to weld the samples to the E-chips. It also resulted in the purchase and installation of an ex-situ lift out station at Drexel. This purchase enabled the project to move forward, as it solved the problem is placing FIB prepared samples onto the E-chips, as once the used is familiar with both the FIB sample and the E-chip design and limitations the success rate for placing samples is near 75%. In addition, as will be discussed later, this tool opened up the opportunity to cross-section the FIB samples following oxidation so that additional information could be gained from the samples.

2.2.3: Initial *In-situ* Oxidation Experiments:

Following the development of a suitable technique for preparing samples on the E-chips, oxidation experiments began, with the first step being the refinement of the oxidation parameters, as the parameters used for a thin TEM sample were expected to be significantly different from a bulk sample. The first experiment run on a Zircaloy-4 sample appeared to showed no oxidation of the Zry-4 in a static 20% oxygen environment in temperatures ranging from 360°C up to 450°C. Based on the results of that in-situ corrosion experiment, a successful experiment was conducted in an atmosphere of 50% oxygen at a temperature of 800°C. Figure 3 shows the initial condition of the sample used for this experiment.

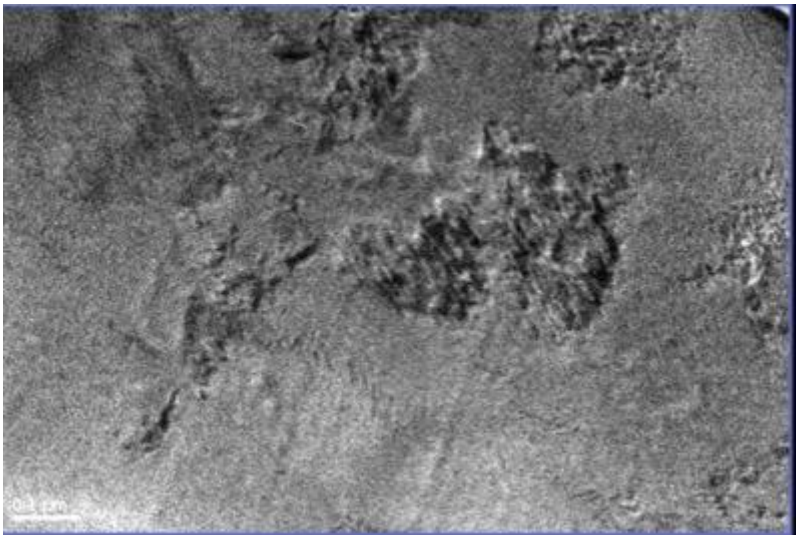

Figure 3: Beginning of in-situ oxidation experiment in Zry-4

For this experiment, the sample was heated for 40 minutes in the given environment. Initial expectations were for larger scale corrosion to occur, so relatively low magnification was used to monitor the experiment. Figure 4 shows TEM images taken during the oxidation process, at times of 10 minutes and 30 minutes.

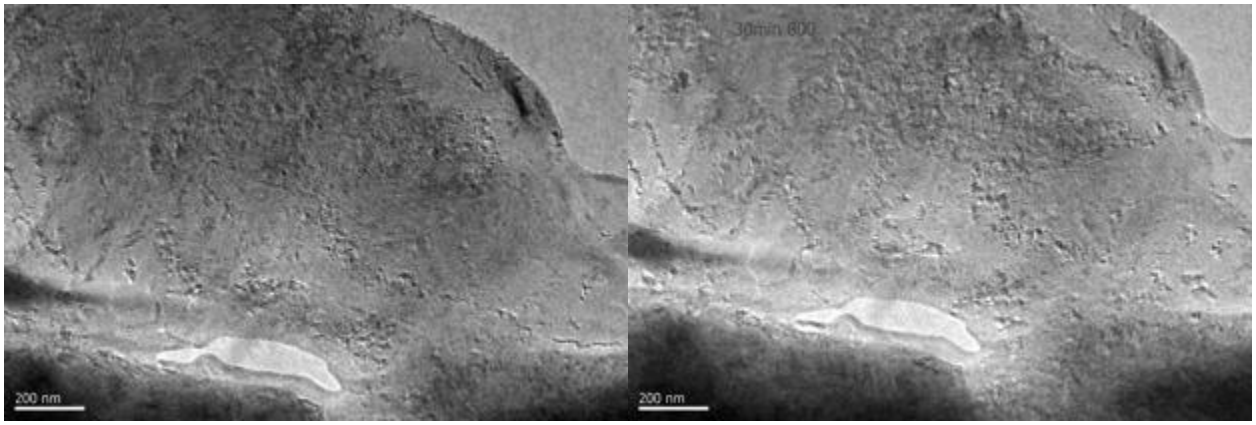

Figure 4: TEM images showing the oxidation of Zry-4. These images were taken after 10 minute at 800°C (right) and 30 minutes at 800 °C (left).

After 40 minutes at 800°C with little visible change being seen in the sample, higher magnification was used to better examine the sample. As seen in Figure 5, significant changes had occurred which were not observed at the lower magnification. These images show what appears to be oxidation of the sample. Later analysis utilizing the Nanomegas precession diffraction system identified this phase as mostly monoclinic ZrO_2 as is seen in figure 6. This lead to a change in imaging conditions, with future in-situ experiments will be undertaken at higher magnification due to the size of the features found after this experiment.

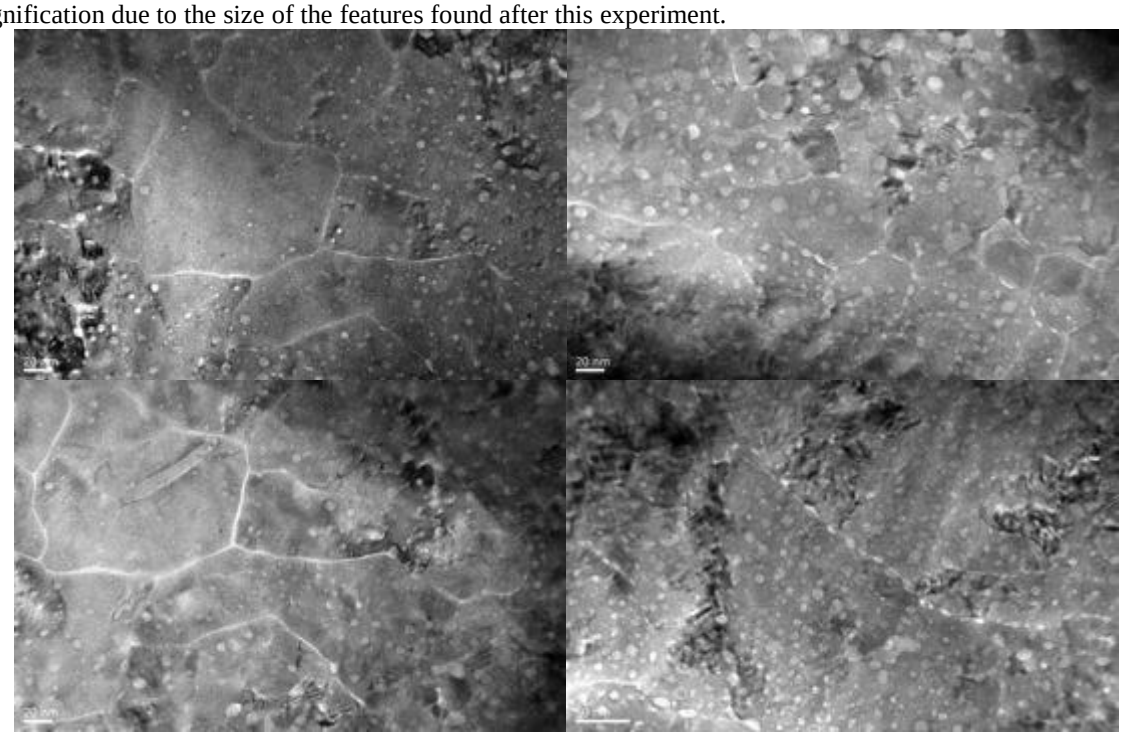

Figure 5: Higher magnification images of the Zry-4 sample following 40 minutes at 800°C taken from multiple locations.

Following this success, the samples used in the successful in-situ experiment were also studied using the Nanomegas system. As can been seen in Figure 6, the majority of the sample consists of monoclinic ZrO_2 following the in-situ oxidation experiment. At this point, it was determined that the best option for characterizing these samples following oxidation was to remove the sample from the E-chip, which would remove the background noise from the SiN window, so that higher resolution imaging could be achieved.

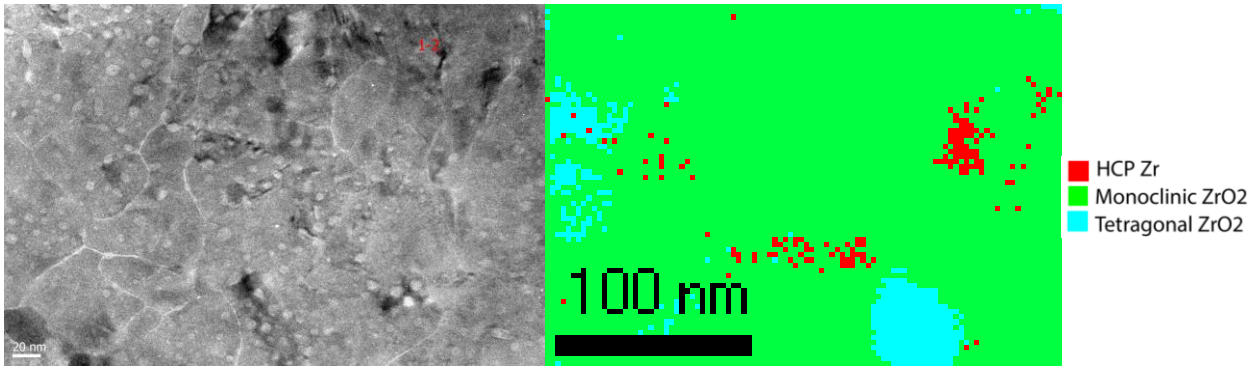

Figure 6: TEM image (on left) showing the region over which the Nanomegas scan was taken to create the phase map (on right).

Following the successful use of precession diffraction to determine phases in the post-oxidation in-situ sample, work continued on how to use this technique on samples already on E-chips for pre-oxidation characterization. The solution was that gas line plugs for the in-situ holder were acquired, which allow for use of a single window instead of a two windows in the in-situ holder. This has made it possible to use the Nanomegas system at Drexel for phase mapping prior to the experiment, as well as post experiment with the sample remaining on the E-chip. Figure 7 shows a TEM image for a pristine sample on the left showing a grain boundary, a phase map for the image area, and on the right is a misorientation map. In the phase map, red indicates HCP Zr, Blue indicates tetragonal ZrO_2, and Green indicates monoclinic ZrO_2. This pristine sample shows to be entirely HCP Zr, with a grain boundary having a disorientation of ~22°.

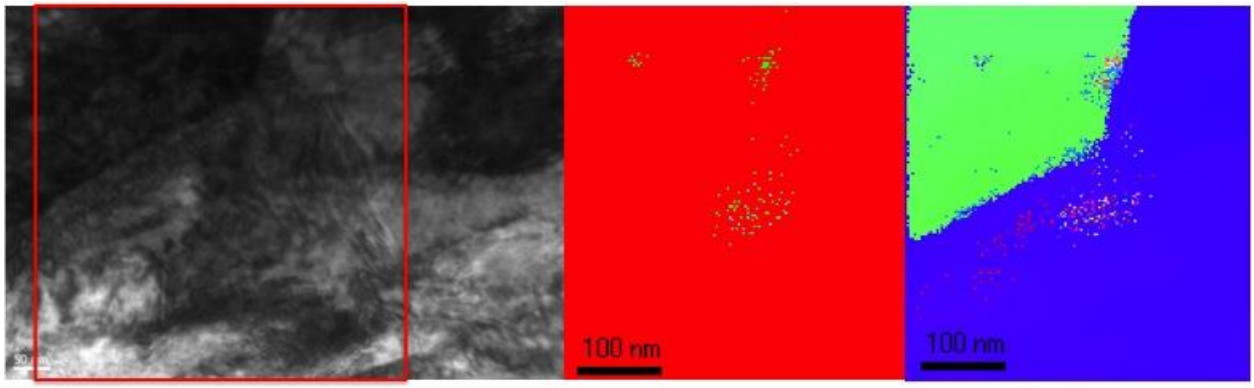

Figure 7: Bright field TEM image (on left) showing the approximate area (red box) from which the phase map (center) and orientation map (right) were generated using Nanomegas.

In addition, Nanomegas is being used to characterize both in-situ and ex-situ corroded samples. Figure 8 shows a comparison of the bright field TEM images and phase maps for these two samples. The top two images show the in-situ sample, TEM image on the left, phase map on the right. The lower two images are from the ex-situ autoclave corroded sample, with TEM image on the left, phase map on the right. For both samples, the same key as in Figure 7 applies, red is HCP Zr, green monoclinic ZrO_2, and blue tetragonal ZrO_2. From these phase maps, it is easy to see that the phases present in the in-situ sample correlate very well with the phases present in the ex-situ sample.

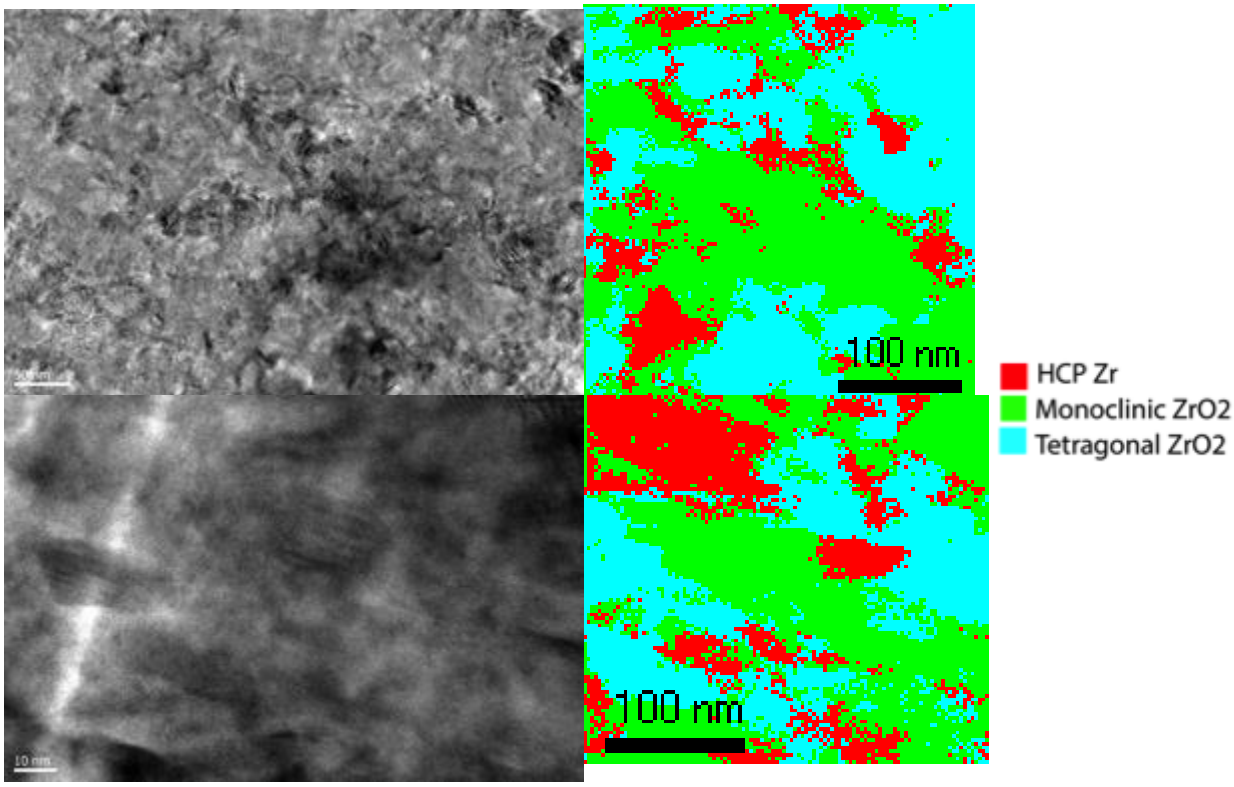

Figure 8: TEM images and corresponding phase maps for in-situ and ex-situ corroded samples. The in-situ sample is represented by the top two images, the autoclave corroded sample is shown in the bottom two images.

2.2.4 Development of a Cross-sectioning Technique for FIB prepared Samples and Oxidation Parameter Refinement:

At this point, all the information gathered pointed toward the need to further refine the parameters for in-situ TEM experiments. To this end, in-situ TEM experiments continued, with the precession diffraction being used to map both phases and boundaries in the sample prior to the experiment and immediately following the experiments to try and determine ideal oxidation parameters. However, at this point there was still a lack of information in the Z direction of the sample, meaning that oxidation depth could not be determined, nor could it be determined if grain structure was equiaxed or columnar since the growth direction was parallel to the electron beam in the TEM. The needs for this depth and grain structure information lead to the development of a technique to make a cross-sectional sample from the in-situ sample. Initially, this technique was developed using a titanium sample from a rapid heating experiment so as not to waste a valuable in-situ sample. Figure 9 shows an overview TEM image of the layers in the completed sample (left) and a higher magnification image showing the appearance of the resulting film area.

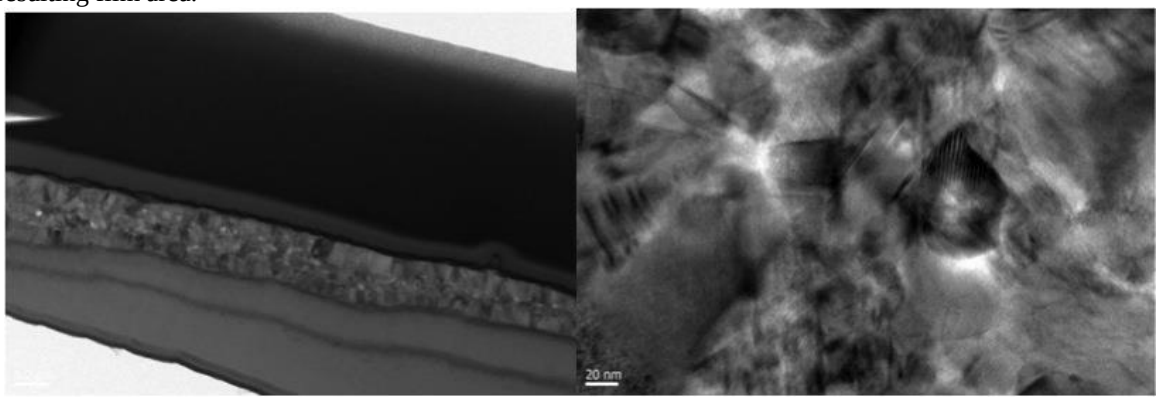

Figure 9: Overview TEM image showing a cross section from a thin Ti TEM sample. Image on the right shows a higher magnification image of the cross section of the sample.

This allows for phase maps showing the depth of the oxide formation in the in-situ sample. Figure 10 shows a TEM image on the left from the area the phase map on the right was produced. As can be seen, this sample has been oxidized through thickness, with both tetragonal and monoclinic ZrO_2 having formed in the sample. Due to this development, the in-situ experiment parameters will be changed, so that the oxidation process will be stopped sooner, in hopes of not having through thickness oxidation.

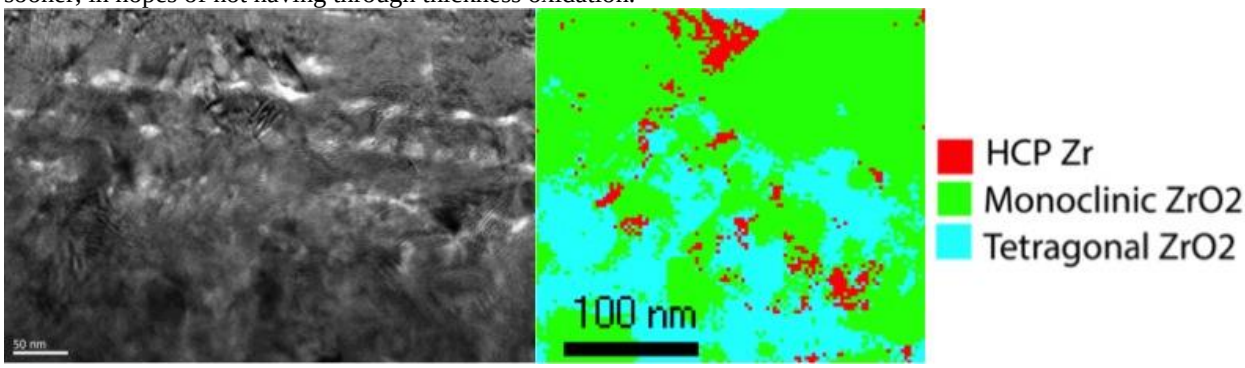

Figure 10: TEM image of the cross section from an in-situ sample and the corresponding phase map showing through thickness oxidation of the in-situ TEM sample

In parallel with this work, many other experiments have been conducted to test the environmental holder, including oxidation experiments in 2D Ti_3C_2 to from TiO_2, which resulted in a paper published by Journal of Materials Chemistry A, and some initial tests on heating of liquid-based samples to precipitate carbides.
After the development of a technique to make cross sectional samples from the in-situ FIB samples, much time was been devoted to refining the experimental parameters for the in-situ experiments to prevent through thickness oxidation. This process is being conducted by running an in-situ experiment, then after final characterization, cross sectioning the FIB sample and using Nanomegas to create phase maps to determine the oxide layer thickness on the sample. Figure 11 shows the initial plan view phase map, followed by the phase map generated after the in-situ experiment in plan view as well.

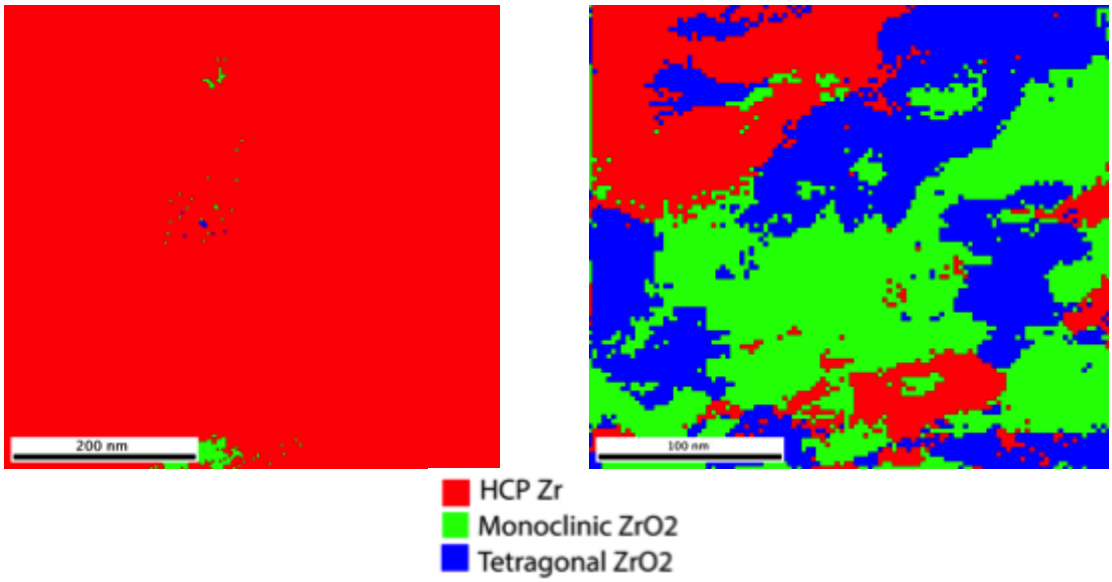

Figure 11: Phase maps for an in-situ sample. On left the phase map for a pristine sample, on right, a phase map for the same sample following an in-situ oxidation experiment

After the experiment seen in figure 11, the sample is cross-sectioned so that oxide thickness can be observed. Figure 12 shows the phase maps from two different areas of the cross-sectioned sample along with the corresponding TEM images. It can be seen that both the oxide thickness and the oxide structure varies across the sample. This may be a result of different grain orientations in the sample.

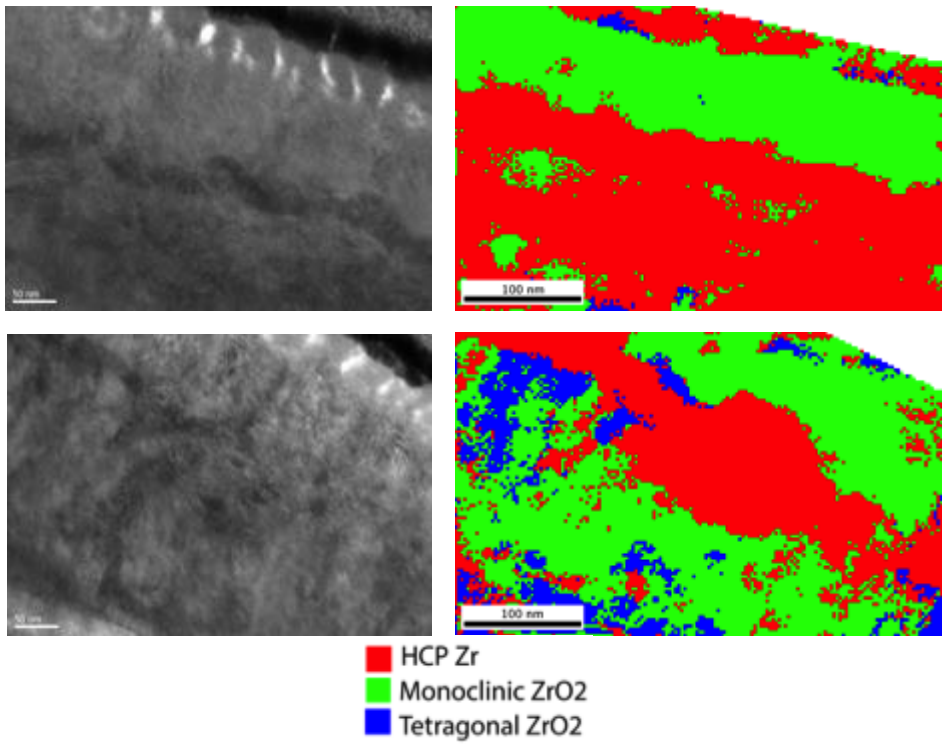

Figure 12: TEM images and corresponding phase maps for two different areas from a cross section of the sample seen in figure 11 showing oxide thickness and phases present.

These results showed that it is possible to refine experiment parameters to reduce through thickness oxidation, however based on phase mapping it appears that further refinement is needed for best results on initial stage behavior.

2.2.5 Effect of Grain Boundaries on Oxidation Behavior:

At this point, work on boundary effects on the oxidation behavior of Zircaloy-4 is starting. Figure 13 shows example images from a pristine FIB prepared sample for these oxidation experiments. This sample contains multiple clear boundaries of varying type, as is seen in the orientation maps, with the entire phase map showing pure HCP zirconium..

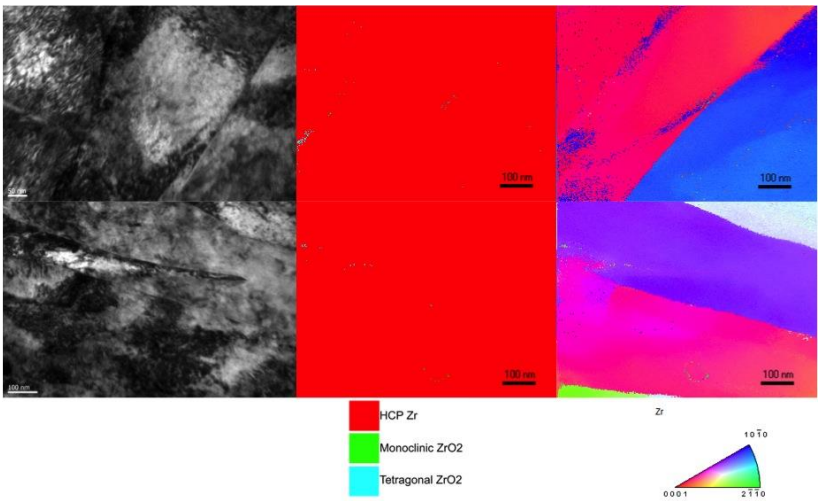

Figure 13: Bright field TEM image with corresponding phase and orientation maps resulting from precession diffraction scans showing multiple grains present in a FIB sample.

These samples will be oxidized in-situ, and then effect of boundaries on the oxidation behavior of the sample is being studied, however at this point work shifted for focus on pure zirconium to provide a better model system as it had been shown that oxidation behavior between autoclave and in-situ TEM were similar in the more complex case. A paper on the successful replication of autoclave oxidation via in-situ TEM was accepted to the Journal of Nuclear Materials. This work shows that in-situ TEM can be used to effectively oxidize a FIB prepared sample while observing the sample, and that the oxidation process closely resembles the oxidation behavior as seen in the autoclave.

Pure Zirconium samples in both the pristine and autoclave-oxidized condition provided by PSU. Initial characterization is ongoing on these samples. Figure 14 shows example images from a pristine FIB prepared pure Zr sample for in-situ oxidation experiments. Does not appear to have a boundary in the field of view, as is seen in the orientation maps, however the entire phase map showing pure HCP zirconium.

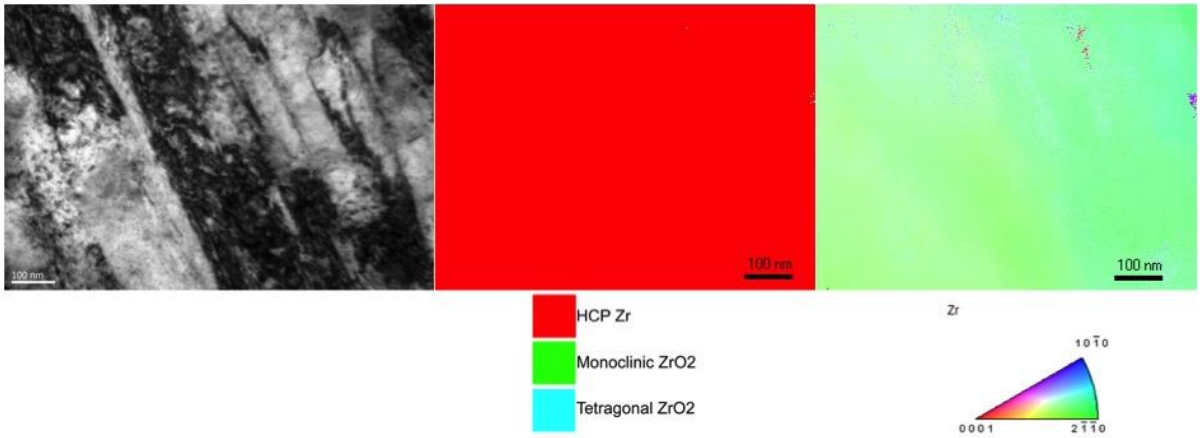

Figure 14: Bright field TEM image with corresponding phase and orientation maps resulting from a precession diffraction on a pure Zr FIB sample.

In a similar process to that used for the Zry-4 samples, these samples are then being oxidized in-situ, and the conditions for in-situ oxidation of pure Zr versus Zry-4 were being studied. It was found that, as expected, the oxidation of pure Zr is much quicker than for Zry-4, and oxidation conditions were adjusted by lowering the exposure time to account for this difference. In addition, as discussed later, humid environment development for the TEM holder is underway, and comparisons between dry gas and humid environments will soon be conducted. Following this, work on boundary effects will continue using the pure Zr samples to remove alloying element effects from the oxidation behavior. In addition, after the installation of a new TEM at Drexel that will allow access to both energy filtered TEM and high angle annular dark field techniques, boundary effects should be easier to discern as these techniques should allow for improved contrast between base metal and oxide during the in-situ experiment.

2.2.6 Study of Stress-stabilization of Tetragonal ZrO_2 in FIB-prepared Samples:

With the arrival of the autoclave-oxidized pure Zr, it was decided that based upon the differences in results between plan view and cross sectional precession diffraction following in-situ experiments, a short study on the stress stability of tetragonal versus monoclinic ZrO_2 in thin TEM foils should be undertaken. Specifically, there is concern that when a FIB prepared sample is thinned beyond a critical point, all the tetragonal ZrO_2 will relax into monoclinic ZrO_2. To study this, a FIB prepared sample with multiple thicknesses is being prepared to look for changes in phases present. A schematic showing the sample appearance is shown in figure 15.

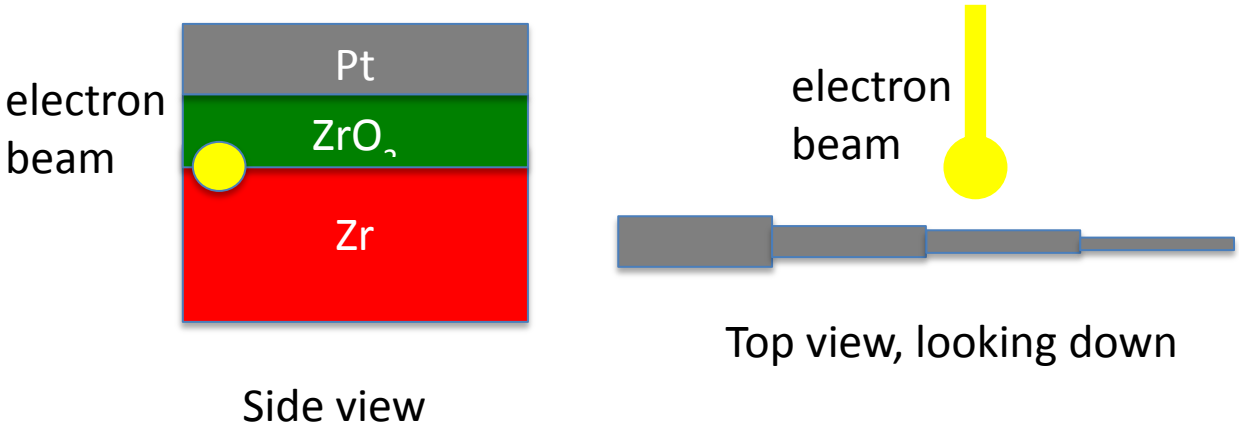

Figure 15: Schematic showing the appearance of a sample used for studying the stability of a tetragonal ZrO_2 in thin TEM samples.

Precession diffraction was used to determine the phases present in the various thicknesses of the autoclave-oxidized sample. The initial results of this study, shown in figure 16, illustrate that there does appear to be a thickness at which the tetragonal ZrO_2 phase is no longer stabilized in the TEM sample. In the thinnest region of the sample, there appears to be almost no tetragonal ZrO_2 while in the next thickest step there is a significant amount of tetragonal present in the sample. The thickness difference in these two areas of the sample still needs to be quantified, and this will be done once the installation of Drexel's EELS capability is complete. Multiple samples have shown similar behavior in this regard, and are awaiting EELS to quantify thickness variation between each step. In addition, a collaboration with Simon Phillpot's research group at University of Florida to correlate TEM results for stress stability of tetragonal ZrO_2 with DFT has started.

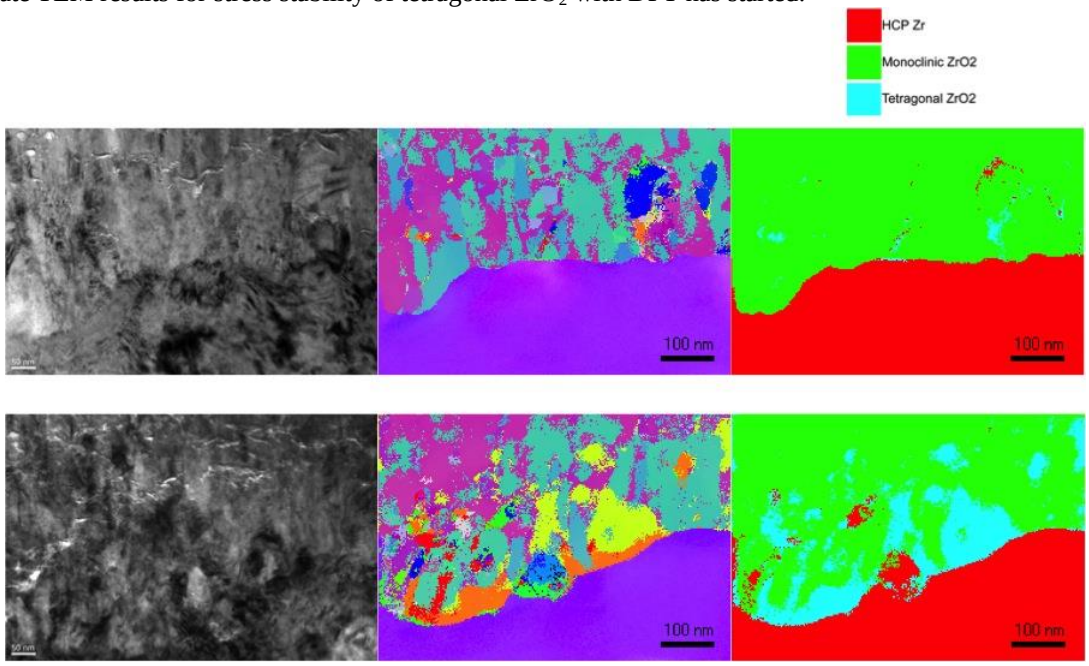

Figure 16: TEM images and corresponding precession diffraction scans showing the stability of tetragonal ZrO_2 in TEM samples. The top row of images shows the results from the thinnest section of the sample, while the lower row shows the sample information for a thicker region of the sample.

2.2.7 Development of High Humidity Environments for In-situ Holder:

Work is ongoing for quantification of the humidity in the environmental cell in preparation for running oxidation experiments in humid environments. The material selected for these initial studies is soot, as soot collects and forms chains of small particles that when exposed to high humidity environments collapse and densify. Figure 17 shows some examples of these particles in the uncollapsed state.

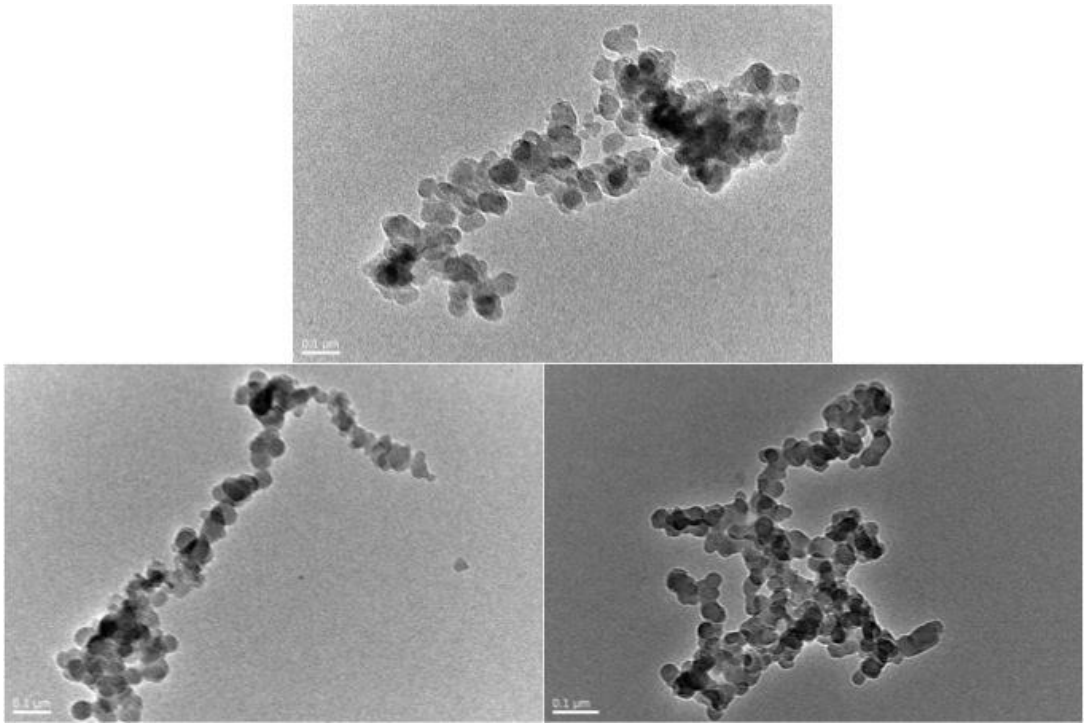

Figure 17: TEM images showing the initial morphology of soot particles intended for humidity testing of the environmental cell holder

Hydroscopic salts are also being investigated as another possible material to use for studying humidity effects, due to both repeatable cycling of the salt, and significant size changes when critical humidity levels are reached. Work to develop a suitable system for introduction of humid atmospheres into the environmental holder continue, and initial testing has commenced. These initial tests have shown that better control over the humidity levels coming into the holder needs to be achieved, as currently overshooting the desired humidity levels is a problem. However, initial results for salt experiments are promising that high levels of humidity are reaching the sample area of the holder. One corrosion test was done on a pure Zr sample, and it was found to be much more aggressive than a dry gas environment, with oxidation starting prior to an increase in temperature.

3.1 Conclusions:

An in-situ TEM technique has been developed that allows for the study of the first stages of corrosion behavior in real time at high resolution. Sample preparation for this technique has been mastered, and a wide variety of environments can be simulated, most recently a wet air environment has been developed. In addition, modifications have been made to make the TEM sample holder compatible with precession diffraction, allowing for phase and orientation information from the sample to be easily accessed. By using this technique, it has been found that behavior similar to autoclave oxidation can be seen in-situ in the TEM if full sample oxidation occurs, including both phases present in the oxide, oxide structure, and cracking behavior. At shorter times, it is possible to observe the initial oxidation processes, and to determine where oxidation first occurs. This allows for the determination of the effect of microstructural features such as grain boundaries and secondary phase precipitates.

3. Experimental – Interfacial Studies From Bulk Techniques to Atom Probe Tomography

1. Introduction

Zr-based alloys are widely used as cladding materials in nuclear power plants because they are essentially transparent to neutron. They also show adequate mechanical behavior and reasonable corrosion resistance in common media. However in the high temperature aqueous environment in a power reactor (300-400ºC at around 15 MPa), waterside corrosion remains the limiting factor of the lifetime of fuel components. Since economic factors have driven the operation of nuclear power plants to higher coolant temperatures, longer operating cycles, and longer in-reactor residence times, waterside corrosion has become a critical safety issue. Alloys with greater corrosion resistance are required to ensure plant reliability for extended times at these hasher conditions[1].

The rate of oxidation of any material is usually evaluated by measuring the increase in weight due to oxygen incorporation as a function of exposure time. For most Zr alloys, the corrosion rate evolves during the corrosion process; it decreases over time as the oxide scale forming on the surface creates a layer protecting the underlying metal from further oxidation. At some point in time, a transition, called breakaway transition, occurs, which is accompanied by a sudden increase in corrosion rate and the loss of oxide protective nature. Depending on the alloying elements, different Zr alloys can exhibit huge differences in oxidation kinetics, as illustrated in **Figure 1**. Zircaloy-4, a commercial alloy, shows oxide growth behavior with well-defined periodic transitions. The oxide formed on pure Zr loses protectiveness right away, while that formed on alloy Zr-Fe-Cr, (an alloy created by arc melting small amounts of Fe and Cr with Zr), show protective behavior for the whole duration of the test.

What makes this plot particularly puzzling is that the differences in amounts of alloying elements between these alloys are very small, yet their behaviors run the gamut from totally protective to immediately non-protective.

Work scope

To address these differences and potential reasons for the different behaviors, the work at the U. of Michigan was divided into 3 tasks:

1 – Oxide and sub-oxide scale characterization as a function of corrosion time for different Zr alloys exhibiting very different corrosion rates.

2 – Atom Probe Tomography (APT) characterization of solute distributions within the alloy, oxide, and suboxide phases.

3 – Characterization of the early stages of corrosion of understand the possible microstructural features associated with the onset of breakaway.

2. Materials and Methods

The alloys studied were crystal bar Zr, Zircaloy-4, and Zr-0.4Fe-0.2Cr. The nominal chemical compositions of the alloys were measured by vacuum hot extraction and are given in **Table 1**.

Table 1 Chemical composition of Zirconium alloy ingots as measured by hot vacuum extraction and matrix composition as measured by APT. Errors of APT measurements are calculated from dataset to dataset variations and counting statistics within each dataset.

Alloys		Sn	Fe	Cr	O	C
Crystal bar Zr	HVE (wt.%)	<0.002	0.009	<0.0005	<0.025*	0.014
	HVE (at. %)	<0.002	0.015	<0.002	<0.14	0.11
	APT (at. %)	N.A.	0.002 ±0.001	0.002 ±0.001	0.032 ±0.002	0.008 ±0.001
Zircaloy-4	HVE (wt.%)	1.32	0.19	0.094	0.131	0.015
	HVE (at. %)	1.01	0.31	0.16	0.74	0.11
	APT (at. %)	0.99 ±0.03	0.003 ±0.002	0.015 ±0.010	0.9 ±0.03	0.07 ±0.04
Zr-0.4Fe-0.2Cr	HVE (wt.%)	<0.002	0.38	0.22	0.112	0.021
	HVE (at. %)	<0.002	0.61	0.36	0.63	0.16
	APT (at. %)	N. A.	0.004 ±0.002	0.015 ±0.002	0.68 ±0.002	0.04 ±0.002

* Oxygen value below lowest verifiable calibration point

Coupons of these alloys were autoclave corroded in 360°C water following ASTM Practice (G2-88) as part of a previous research project[2, 3]. The corrosion behavior was evaluated by measuring the weight gain versus exposure time curve, as shown in **Figure 2**. This is possible because the oxide is adherent, does not dissolve, and almost all the oxygen is used to form oxide so that there is very good correspondence between weight gain and oxide thickness such that Column 3 is obtained by diving the weight gain by the factor 14.5. The alloy samples used in this work are listed in **Table 2**. All of the three samples examined in this study were in the protective regime.

Quantitative measurements and descriptions of solute element distributions can be extremely difficult by traditional experimental techniques. We use atom probe tomography (APT) in combination with transmission electron microscopy (TEM), scanning electron microscopy (SEM), and electron backscattered diffraction (EBSD).

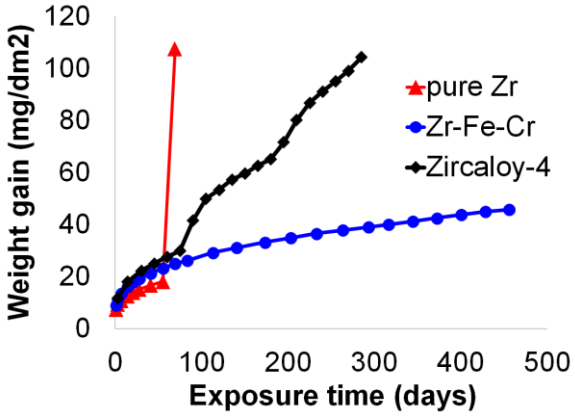

Figure 1: Corrosion weight gain-exposure time for studied alloys oxidized in 360°C water.

Table 2 Corrosion tests conditions of studied alloy samples

Studied Alloy	Exposure Time (days)	Weight Gain (mg/dm^2)	Calculated Oxide thickness (μm)
Crystal bar Zr	1	6.9	0.5
Crystal bar Zr	7	10.5	0.7
Zircaloy-4	60	27.6	1.9
Zircaloy-4	90	41.7	2.8
Zr-0.4Fe-0.2Cr	7	14.4	1.0
Zr-0.4Fe-0.2Fe	60	24.6	1.7
Zr-0.4Fe-0.2Cr	456	45.6	3.1

Cross-sectional samples were cut from the oxidized coupons, glued on a metallic support using crystal bond, and ground on 1200 grit SiC paper on both cross sectional sides. One side of the sample was polished using successively finer polishing cloth to 0.5μm diamond. The needle-shaped samples for atom probe tomography were prepared using a focused ion beam (FIB)-based lift-out method, which allowed to selectively extract volumes which contained metal/oxide interfaces. APT samples with different orientations of interfaces (either parallel or perpendicular to the needle axis) were fabricated to better investigate both the interface region and the oxygen ingress into metal (**Figure 2**). Pt was deposited as a protective layer and the standard lift-out procedure[4] was applied. A final 2kV clean-up procedure was utilized to remove any remaining Pt and to minimize the Ga damaged region.

The lift-out samples were analyzed using a CAMECA LEAP-4000XHR operated in a laser pulsing mode with 200 kHz pulse repetition rate and 70-100 pJ laser energy. The temperature of the specimens was maintained at 50 K while the standing voltage was varied automatically to maintain a detection rate of 0.005 ion/pulse. The collected data was reconstructed and analyzed using the IVAS reconstruction software (need reference). The default value of the image compression factor (3.3) and the evaporation field of Zr (28V/nm[5]) were selected for reconstruction. The composition measurement was done separately for each phase and a peak decomposition technique was used to deconvolute the Zr^{3+} peak from the O_2^+ peaks, which overlap at 32 mass-to-charge ratio.

All the following composition results derived from APT are given in atomic percent.

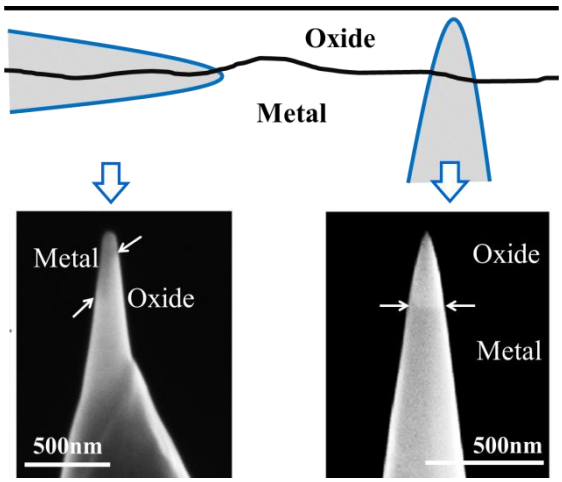

Figure 2: Schematic illustration and SEM images of the two orientations chosen for the APT specimens

3. Chemistry of the starting alloys

3.1. Crystal bar

APT samples taken in the bulk of the alloy, i.e. far away from the oxidized surface (~200 µm), show a generally uniform distribution of Cr without any evidence of clusters or indication of elemental segregation to microstructure features such as grain boundaries or dislocations. No Fe was detected in this volume – note that the detection limit for Fe was about 0.002 at. % (12 wt ppm). Concentration measurements from the APT datasets matched the Zr and Cr concentrations measured using hot vacuum extraction as shown in **Table 1**. Small amounts of C, O and Al were also detected. The low Fe concentration measured in the matrix is reasonable. The alloy is in a recrystallized state with a final heat-treatment temperature corresponding to an extremely low solubility of Fe in Zr. The reported maximum solubility of Fe in α-Zr is 120 wt ppm (0.02 at. %) at 800 ºC and less than 50 wt ppm at temperatures lower than 300ºC. Fe is found to be segregated to grain boundaries, as illustrated in **Figure 3**. Segregation of the other elements (Cr, C, O and Al) is not observed on the grain boundaries. Cr is a slower moving diffuser in Zr than Fe so the result is not surprising. It is expected that if APT were to be performed over a representative volume of the microstructure containing regions of high iron concentration the values would match.

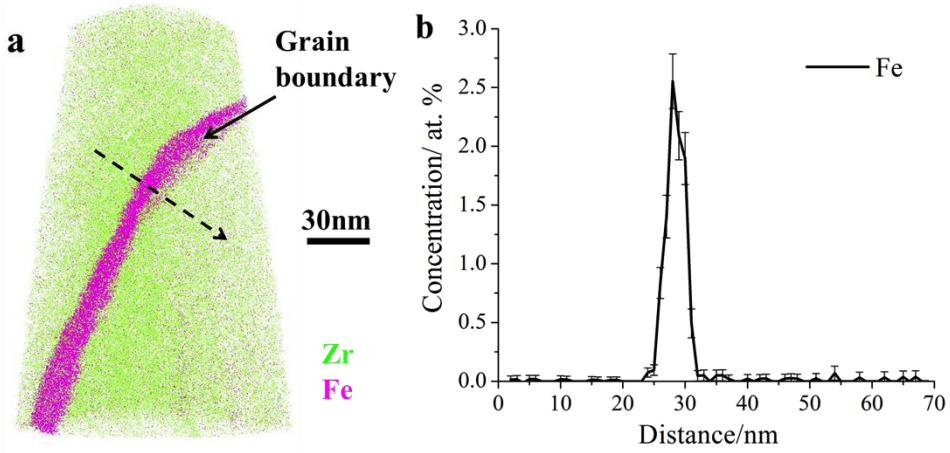

Figure 3: Bulk crystal bar Zr: (a) APT reconstruction showing a grain boundary with Fe segregation; (b) line profile across grain boundary along the arrow shown in (a).

3.2. Zircaloy-4

Zircaloy-4 contains Sn, Fe and Cr as major alloying elements. Sn is found in solid solution and Fe and Cr mostly in intermetallic precipitates of the type $Zr(Cr,Fe)_2$. The matrix Sn concentration was measured from the bulk of the metal far away from the oxide, and calculated from a dataset without grain boundaries and clusters (**Table 1**). The Fe and Cr matrix concentrations determined by APT were close to the reported solubility limits (0.04 at. % for Cr at 860ºC and 0.02 at % for Fe at 800ºC), which are much lower than the bulk alloy concentration, since essentially all Fe and Cr are in precipitates. The Sn concentration was in the range of expected value.

The average spacing between precipitates (usually 0.1-0.3µm in size) in recrystallized Zircaloy-4 is greater than 1µm, so their capture in the APT specimens is unlikely. However, some small clusters (~ 5 nm diameter), which would normally be invisible in TEM are occasionally seen by APT, as shown in **Figure 4(a).** The apparent composition of these clusters is obtained from a proxigram analysis based and is 89.3±1.9% Zr, 4.8±1.3% Fe, 5.9±0.7%Cr. However, these numbers are affected by ion trajectory aberrations from the difference in evaporation fields between matrix and clusters, as evidenced by the apparent higher density of ions observed at the position of the clusters.

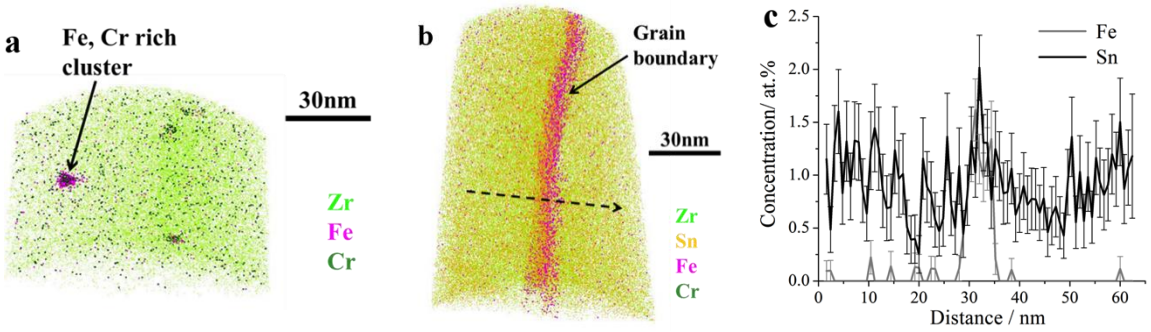

Figure 4: Bulk Zircaloy-4: (a) APT reconstruction showing Fe,Cr rich clusters; (b) APT reconstruction showing grain boundary with Fe and Sn segregation; (c) line profile across grain.

Fe and Sn segregation was observed at grain boundaries (**Figure 4(b)**). A line profile of concentration through the grain boundary in **Figure 4(c)** shows noticeable segregation of Fe (up to 1.5% or a enrichment factor of 5 relative to the alloy bulk and much higher relative to the Fe content in the matrix (**Figure 4(c)**). A much less marked segregation of Sn can also be discerned in the same figure. No Cr segregation of other elements was seen on the grain boundary. The results slightly differ from with *Hudson et al.*[6], where no Sn were observed on grain boundaries of ZIRLO alloy. It also differed from a more recent APT study[7] on Zr-Cr binary alloys in which Cr segregation at grain boundaries was observed. The differences in alloying element distribution are attributed to different alloy composition and processing history.

3.3. Zr-Fe-Cr

As shown in **Table 1**, the measured matrix concentrations of Cr and Fe in the bulk of the alloy are much lower than the overall alloy composition, likely because most of the Fe and Cr are usually found in C14 $Zr(Cr,Fe)_2$ Laves phase precipitates. A portion of one such precipitate was caught in one of the needles, as seen in **Figure 5**. The measured atomic composition of 34.50±0.11% Zr-43.68%±0.10Fe-21.82±0.08%Cr, is in reasonable agreement with the overall stoichiometry of the $Zr(Cr,Fe)_2$ Laves phase. Similarly to Zircaloy-4, Fe segregation to grain boundaries is observed to a similar level as in Zircaloy-4 as shown in **Figure 6** and some Al, O and C are also observed in the matrix.

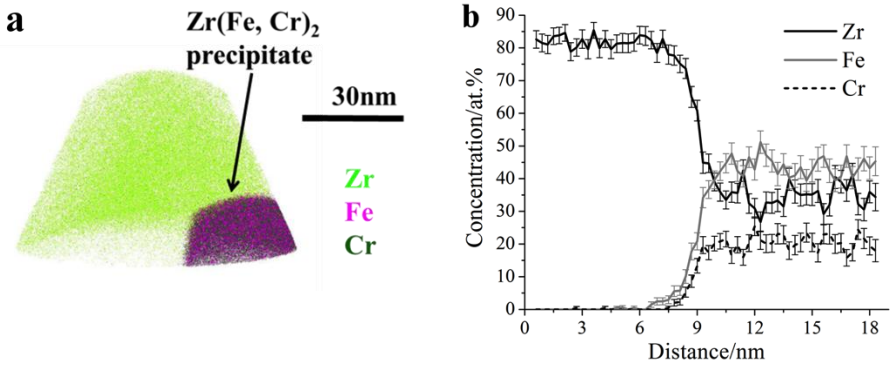

Figure 5: Bulk Zr-Fe-Cr: (a) APT reconstruction showing part of an Fe, Cr rich intermetallic precipitate; (b) line profile across the precipitate interface.

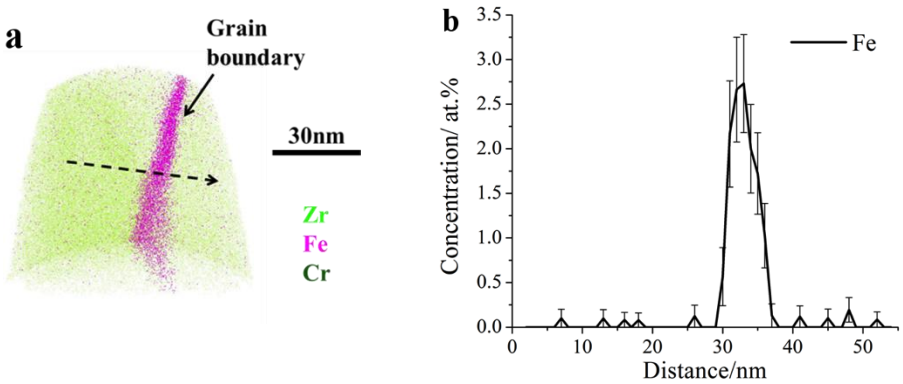

Figure 6: Bulk Zr-Fe-Cr: (a) APT reconstruction showing the grain boundary with Fe segregation; (b) concentration profile across the grain boundary along the arrow shown in (a).

3.4. Summary

The observed alloying element distributions in the bulk of the alloys are consistent with what was known from previous TEM observations and other techniques, with the additional precision of the observation of Fe segregation to lattice defects such as grain boundaries and dislocations and the presence of Fe and Cr rich nano-precipitates. Comparable Fe segregation levels are observed along the grain boundaries of crystal bar and Zr-Fe-Cr.

4. Structure of growing oxide scales on Zr alloys

APT specimens were prepared from the oxide and oxide-metal interface regions in the three alloy samples. ZrO_2 formed as a result of the reaction appears as the oxide layer. A series of oxygen-containing sub-oxide phases are observed for all three alloys. These phases are in order from the oxide metal interface:

(i) the equiatomic suboxide ZrO (both slightly sub and superstoichiometric, denoted here ZrO_{1+x} and ZrO_{1-x}),
(ii) a saturated solution of constant oxygen content at about 30% O, dubbed $Zr(O)_{sat}$, and
(iii) an undersaturated solid solution of O in Zr, the oxygen content of which decreases with distance from the oxide-metal interface.

As stated above, the field evaporation behavior of these phases is drastically different, resulting in characteristic ions being evaporated from each phase. As a result, the phases can be identified both by atomic concentrations and by the nature of the ionic species evaporating from each phase. The latter method was also used to visualize the distribution of phases within needles. For example, it was found in the present study that oxygen was evaporated as O^+, O_2^+, ZrO^{2+}, ZrO^{3+}, ZrO_2^+, ZrO_2^{2+}, ZrO_3^+ with occasional instances of $Zr_2O_2^{3+}$ and $Zr_2O_3^{3+}$ observed. Zr ions (Zr^{2+}, Zr^{3+}) become significant in the $Zr(O)_{sat}$ phase. O_2^+ is only observed in the oxide (ZrO_2) phase, so it is considered a marker for that phase. ZrO_2^+ and ZrO_2^{2+} are present both in the ZrO_2 and ZrO_{1+x} phases but absent in the ZrO_{1-x} phase.

4.1. Crystal bar Zr

A representative APT dataset from a needle prepared containing the oxide-metal interface of a crystal bar Zr sample exposed for 7 days to the autoclave environment is shown in **Figure 7**. A line profile was obtained by integrating the contents of a "tube" perpendicular to the interface, as indicated by the arrow. The resulting oxygen concentration profile taken along the reconstruction axis, shows the composition of the top oxide layer is consistent with that of ZrO_2. The sequence of phases follows the above: an intermediate layer is observed beneath the ZrO_2 layer with a composition corresponding to ZrO (a ZrO cluster is also observed near the ZrO_2/ ZrO interface but inside the ZrO_2 phase). In the metal region adjacent to ZrO, the saturated solid solution layer with 31- 32% oxygen content, $Zr(O)_{sat}$ is observed. The region of undersaturated solid solution follows with a continuously decreasing oxygen profile into the metal. An isosurface with constant Zr concentration is shown in **Figure 7(a)** to show the interface between $Zr(O)_{sat}$ and solid and the same isosurface is used in other figures for the same purpose. The phase diagram shows many ordered phases of Zr(O) solid solution, and it is possible that some of these are present in the distance 70 nm (corresponding to Zr_3O) to 90 nm (approx. Zr_4O) considering the slope changes at that location, but their presence remain to be confirmed. The intermediate oxide layers (ZrO/ Zr(O)sat) in crystal bar Zr are quite thin (less than 20nm).

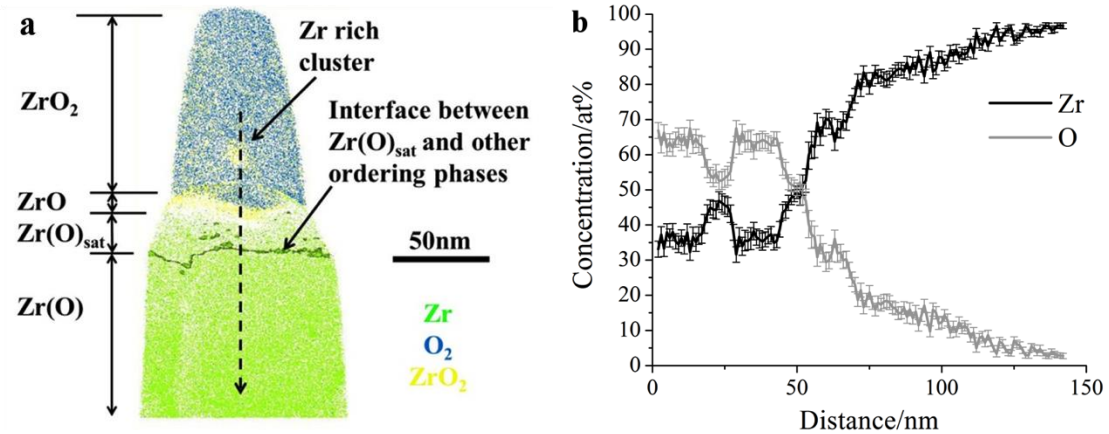

Figure 7: Crystal bar Zr oxide region: (a) a 10nm slice from an APT reconstruction containing the oxide/metal interface; (b) concentration profile along the arrow indicated shown in (a).

The ZrO phase in this sample is not a continuous layer. Along the ZrO/Zr(O)$_{sat}$ interface, small ZrO plates nucleate and align themselves parallel with each other (**Figure 8**).

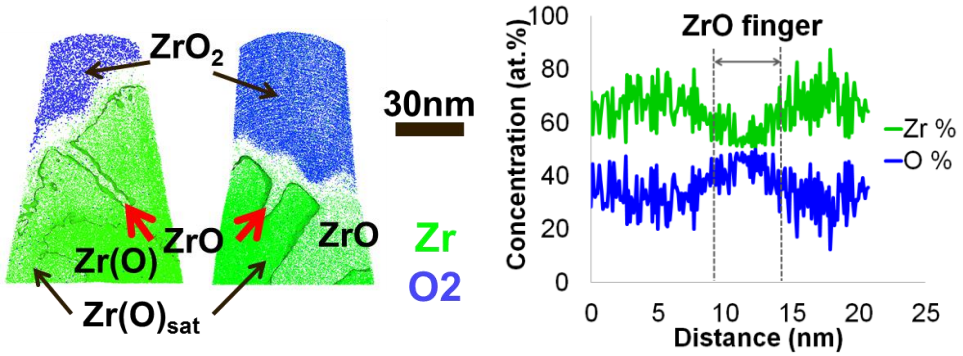

Figure 8: (left) 10 nm slices of two representative APT datasets taken from 7 day crystal bar Zr revealing the presence of ZrO fingers at ZrO2/Zr(O)sat interface; (right) concentration profile of Zr and O across the ZrO finger.

4.2. Zircaloy-4

The examination of a needle taken from the oxide-metal interface of Zircaloy-4 exposed to 60 days to the autoclave environment shows a similar oxide sequence as that seen in crystal bar Zr, but with thicker intermediate layers of ZrO and Zr(O)$_{sat}$. One dataset with interface perpendicular to the tip axis (vertical) and two reconstructed datasets with the interface oriented parallel to the tip axis (horizontal) are given in **Figure 9(a)**. The ZrO layer is about 50 to 100nm thick, and the Zr(O)sat about 100 to 150nm thick. More detailed examination shows that the ZrO layer actually consists of two layers with slightly different compositions, slightly above and slightly below stoichiometry. As seen in **Figure 9(a)**, in this sample also the region represented by ZrO$_{1+x}$ (in yellow) has a composition slightly rich in O while the region denoted ZrO$_{1-x}$ (in white) is slightly deficient in O.

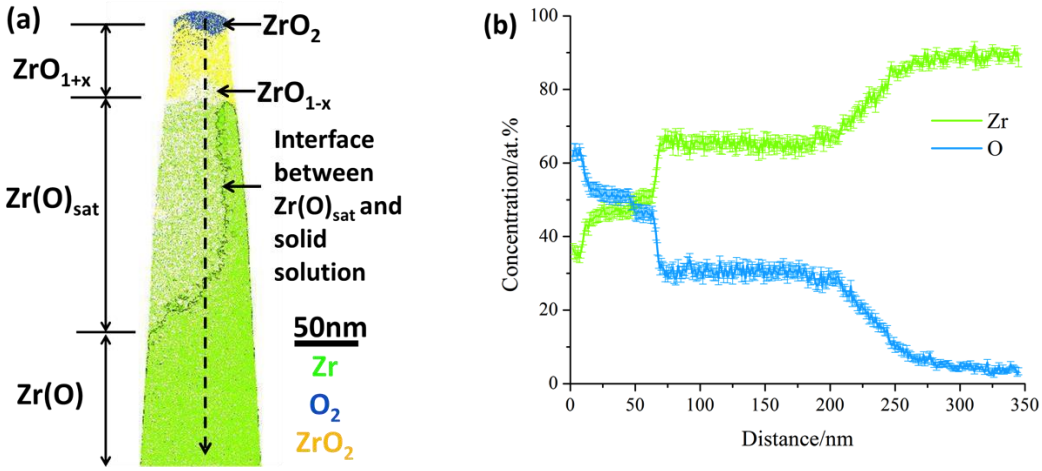

Figure 9: Zircaloy-4 oxide region: (a) 10nm slice from an APT reconstruction showing the presence of different oxide phases; (b) concentration profile taken along the arrow indicated in (a).

In this sample, while the ZrO$_2$/ZrO interface is flat, the interface between ZrO and Zr(O)$_{sat}$ is uneven. For the pre-transition samples, the sub-oxides are generally of variable thicknesses and do not form continuous layers. The

thickness of the ZrO layer varies from 0 to over 80 nm, showing broad semi-elliptical regions of ZrO advancing into a region of $Zr(O)_{sat}$ (**Figure 10(a)**). The Zr(O)sat layer is generally thicker (150–200 nm wide). However variations of the thickness of this layer were observed, indicating that this layer is not continuous along the oxide/metal interface. At transition, the ZrO layer has largely disappeared (**Figure 10(b)**). This difference in the presence of ZrO phase is likely related to the rate of advance of the oxide front. When the rate of advance is high, any fingers of ZrO which serve as precursors of a Zr(O)sat→ZrO transformation are quickly consumed by the advancing front, so that right after transition the fingers are not observed.

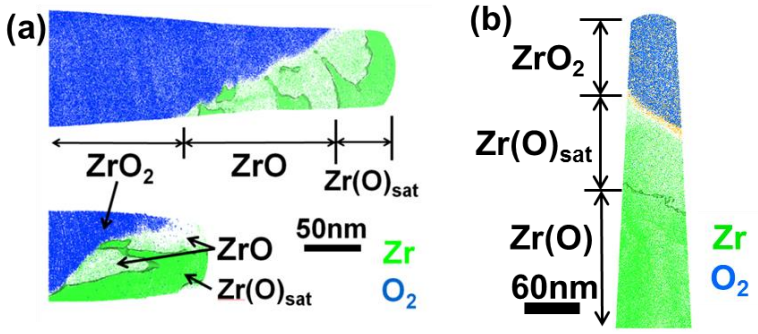

Figure 10: 10 nm slices from APT reconstructions showing the presence of different oxide phases and interface morphologies in (a) 60 days and (b) 90 days Zircaloy-4.

4.3. Zr-Fe-Cr

The same sequence of suboxide and oxide phases seen in crystal bar Zr and Zircaloy-4 is observed in the Zr-Fe-Cr alloy but the phase morphologies evolve differently over time. In the initial stage of oxidation (**Figure 11(a)**), the ZrO phase is not present everywhere between the ZrO_2 and Zr(O)sat phases. Small ZrO plates nucleate at ZrO_2/Zr(O)sat interface, aligning themselves parallel with each other. The ZrO plates then grow to form a continuous layer (**Figure 11(b)**), which grows thicker over time (**Figure 11(c)**).

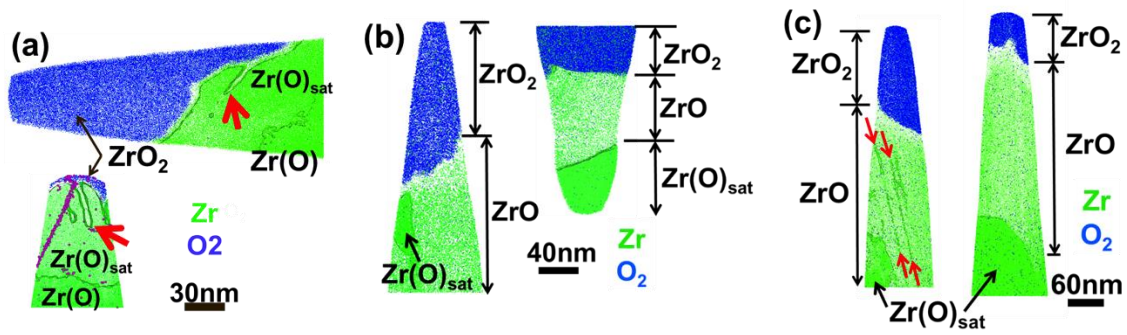

Figure 11: Zr-Fe-Cr oxide region: (a) 10nm slice from an APT reconstruction showing the presence of different oxide phases and oxide morphology; (b) concentration profile along the arrow indicated in (a).

4.4. Field evaporation behavior of the ZrO layer

As observed by APT, the ZrO phase consists of two layers that are either slightly sub- or super- stoichiometric, denoted ZrO_{1-x} and ZrO_{1+x} (**Figure 12(c)**). The ZrO_{1+x} phase is very thin in most cases (<20nm). The interface between ZrO_{1+x} and ZrO_{1-x} always follows the morphology of the ZrO_2/ZrO_{1+x} interface. Observing an oxide phase with a slightly lower O concentration than expected such as ZrO_{1-x} is common in APT analyses, the reason being the lower efficiency of the technique to O ions. Observing a super stoichiometric oxide (ZrO_{1+x}) is more surprising. The morphology of this phase suggests that it could be an artifact resulting from the application of an electric field. The field present in the insulator leads to O migration to interface and reaction of the O ions with the conductive layer. A definite evidence for such an artifact comes from the absence of a ZrO_{1+x} layer when the APT samples are prepared "upside down" so that the metallic layer (ZrO) sits on top of the oxide ZrO_2 as illustrated with specimen 3 in **Figure 12(d)-(e)**. We note that we experienced considerable difficulty analyzing such samples due to the easy fracture of these specimens. Having demonstrated that such ZrO_{1+x} layer is an artifact in some cases, we do not completely exclude that such layer may exist in some location.

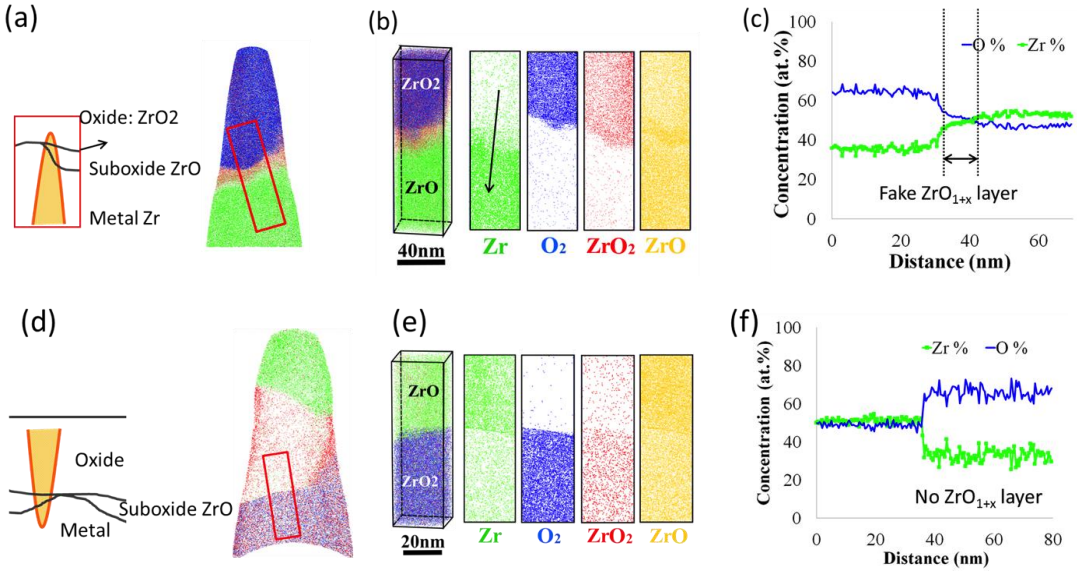

Figure 12: Dependence of the ZrO_{1+x} layer on the APT specimen geometry.

4.5. Summary

Oxide formation in the three alloys showed some similarities. All oxide layers examined showed precursor phases of various oxygen contents. The sequence of phases observed from the oxide water interface to the metal was the same in all alloys, starting with ZrO_2 (corresponding to the traditional oxide layer, which went from the oxide water interface to the oxide metal interface), followed by a sequence of suboxide phases in order:

(i) the equiatomic ZrO phase (observed as both ZrO_{1+x} and ZrO_{1-x}.),
(ii) a plateau of the saturated solid solution $Zr(O)_{sat}$,
(iii) a slowly decreasing oxygen profile, with some hints of specific phases

The slight difference in O concentration could be a field evaporation artifact during APT data collection, but we do not completely exclude that such layer may exist in some location. The present results are in broad agreement with the electron energy loss spectrometry (EELS) measurement[8] and recent first-principle calculation[9].

While the sequence of phases is similar in the three alloys, the layer thicknesses are quite different from one alloy to another and from one stage of the corrosion process to another. In general, the lower the corrosion rate (derivative of the weight gain curve) at the point where the sample was collected, the thicker the suboxide layer, or alternatively,

the more oxygen can diffuse ahead of the oxide. This may be interpreted by considering that the ZrO_2 scale consumes the suboxide layers as it advances, therefore the faster the oxide growth, the thinner the suboxide scale.

The observations of the early stages of corrosion also suggest that while $Zr(O)_{sat}$ readily forms due to the ordering transformation from the solid solution of O in hcp Zr, the formation of the ZrO phase at the interface between the ZrO_2 scale and the suboxide $Zr(O)_{sat}$ may be nucleation limited.

5. Solute distributions near the oxide scale

The distribution of other alloying elements in the metal region next to the oxide, (where significant oxygen diffusion has occurred) is different from that in the bulk of the material. This is reasonable since the phase equilibria should be altered by the presence of oxygen. These results are summarized in this section.

5.1. Crystal bar Zr

Within the oxide and suboxide regions, Fe is found to segregate to the interface between ZrO_2 and ZrO and to grain boundaries in $Zr(O)_{sat}$ and the solid solution region (**Figure 11(a)**). Fe segregation to linear features, possibly dislocations, are observed the region near the oxide metal interface (**Figure 11(c)**). Fe is also found to form clusters on planar features within ZrO_2 (**Figure 11(c)**), possibly as a result of Fe segregation to oxide grain boundaries. Interestingly enough, the Fe segregation on grain boundary extends from metal to the oxide (**Figure 11(d)**). The continuity of Fe segregation is also observed by *Sundell et al.*[10] in Zircaloy-2 with additional Ni segregation on grain boundaries.

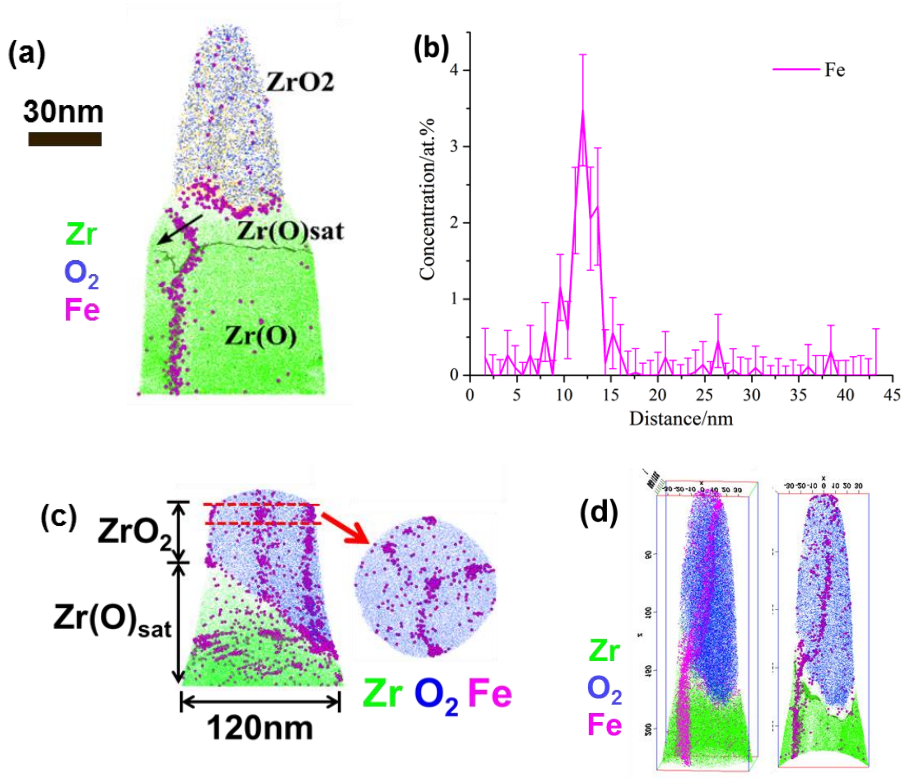

Figure 13: (a) 10 nm slice from an APT reconstruction showing the distribution of Fe at the interface and grain boundary; (b) concentration profiles of across the grain boundary along the arrow indicated in (a); (c) 10 nm slice from an APT reconstruction showing that Fe decorates oxide grain boundaries and dislocations in the metal adjacent to oxide; (d) 3 dimensional atomic maps and 10 nm slice from the same datasets shows the Fe segregation on grain boundary extends from metal to oxide.

5.2. Zircaloy4

The distribution of alloying elements in the oxygen rich region of the metal is more complicated in Zircaloy-4 than in crystal bar Zr. In the $Zr(O)_{sat}$ region adjacent to ZrO suboxide, Fe and Cr-rich fine clusters are occasionally observed (**Figure 14(a)**), indicating a tendency to Fe rejection from the ZrO suboxide phase. Fe is also found to segregate to linear features, possibly dislocations, formed in the region near the oxide metal interface which has

been plastically deformed by the growing oxide (**Figure 14(a)**). The nano-sized Fe and Cr rich clusters and Fe decorated dislocations were also reported by Hudson[11].

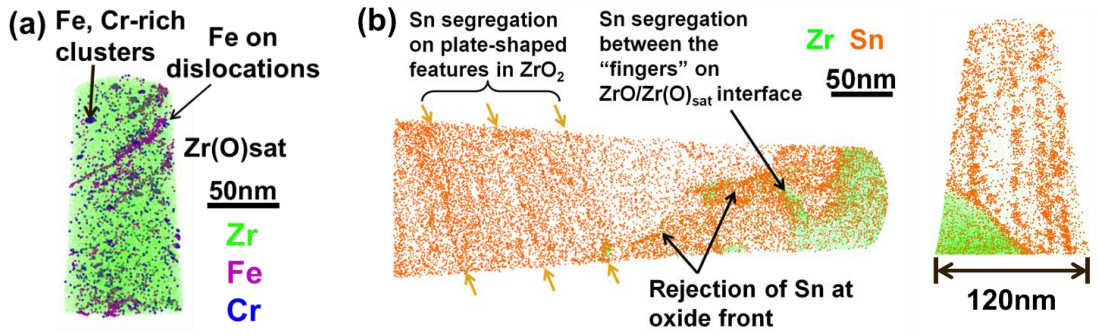

Figure 14: (a) APT reconstruction showing segregation of Fe at dislocations and Fe, Cr rich clusters in Zr(O)sat; (b) 10 nm slices taken from two distinct APT reconstructions showing distribution of Sn.

Segregation of Sn is observed between ZrO and the saturated solid solution $Zr(O)_{sat}$. The segregation to the $Zr(O)_{sat}$/ZrO is strongly dependent on the local curvature of the interface. Higher levels of Sn are observed in the region between the ZrO fingers seen at the interface (**Figure 14(b))** indicating a lamellar like rejection of Sn from the suboxide. Interestingly, Sn also exhibits inhomogeneous distribution within the ZrO_2 oxide layer, to planar type features whose spacing is similar to the measured columnar oxide grain width in these samples, about 30-50 nm, indicating a possible segregation of Sn to oxide grain boundaries**.** Sn clustering and segregation in the bulk oxide was also reported in a more recent APT study[12], where Sn clusters were shown to continue growing to form larger metallic particles as the oxidation proceeds.

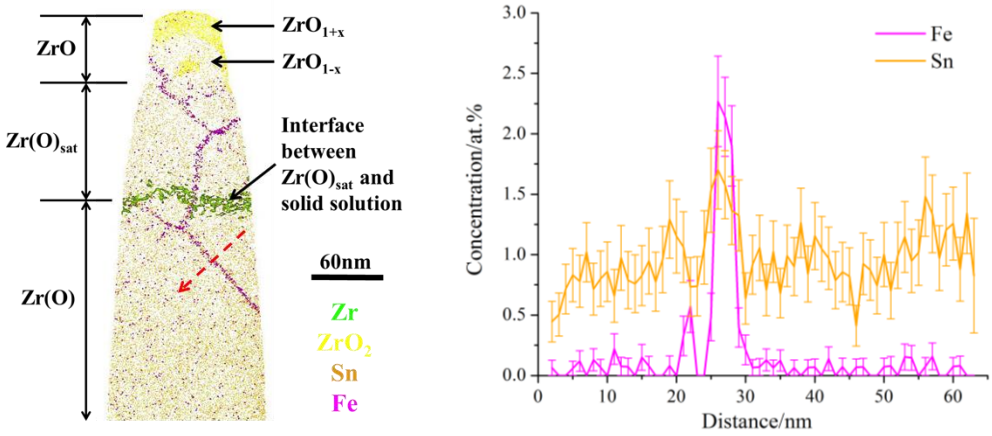

Figure 15: (a) 10 nm slice from an APT dataset shows that Fe and Sn segregate on grain boundaries; (b) concentration profiles for Fe and Sn across the grain boundary along the red arrow shown in (a).

Planar-like segregation of Fe and Sn is also observed beneath the ZrO suboxide layer, indicating possible grain boundary segregation of these elements induced by the oxygen. A slice of the dataset containing grain boundaries is shown in **Figure 15(a)**, along with a concentration profile. The local concentration of Fe (segregation factor) is quite high, (~ 2.5%) (**Figure 15(b)**), to be compared with 0.2% in the alloy and 10s of ppm in the matrix solid solution.

5.3. Zr-Fe-Cr

In Zr-Fe-Cr alloy, Fe segregates to $Zr(O)_{sat}$/ZrO interfaces. Fe is also found to form clusters on planar and linear features within ZrO_2 (**Figure 14(b)**), possibly as a result of Fe segregation to oxide grain boundaries and/or

dislocations. Grain boundaries showing Fe segregation were also observed in $Zr(O)_{sat}$ phase and the Fe segregated to one of the boundaries is still seen segregated in the ZrO phase (**Figure 14(a)**).

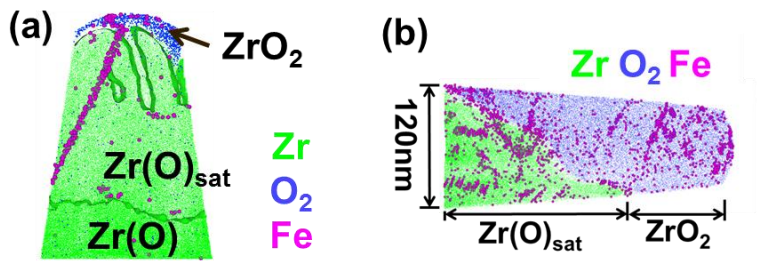

Figure 16: Zr-Fe-Cr oxide region: (a) 10 nm slice one from APT reconstruction showing the Fe segregation at grain boundary of Zr(O)sat; (b) APT reconstruction showing the Fe segregation on dislocations in Zr(O)sat and Fe clustering on planar features in ZrO_2.

5.4. Quantitative Analysis on Grain Boundary Chemistry

It has been hypothesized that differences in grain boundary chemistry (more or less Fe could explain the different stability of oxide layers formed on crystal bar Zr and Zircaloy4. However, as discussed in this section, the Fe grain boundary segregation was similar in the two alloys. Fe segregation was observed at grain boundaries in the $Zr(O)_{sat}$ and Zr(O) phases of pure Zr and ZrFeCr alloy oxidized for 7 days. The segregation levels in this two cases are comparable (**Figure 17)**.

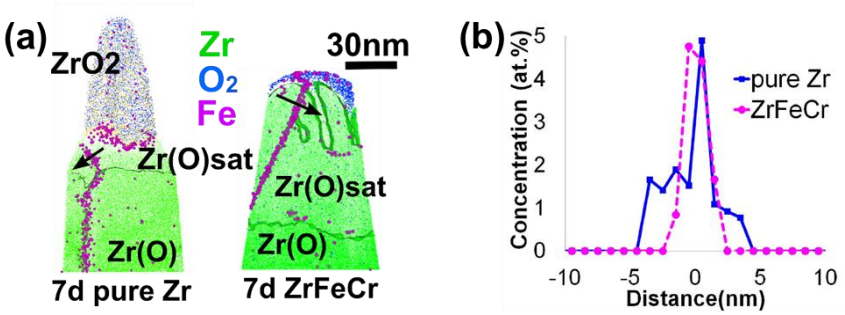

Figure 17: 10nm slices of two APT reconstructions from (a) pure Zr and (b) Zr-Fe-Cr both oxidized for 7 days revealing comparable Fe segregation to grain boundaries as shown in (c).

A detailed quantitative analysis on grain boundary chemistry were conducted for both crystal bar Zr and ZrFeCr, where the Gibbsian excess for each dataset was calculated to evaluate the actual amount of Fe segregation. The Gibbsian interfacial excess Γ_s for solute s is defined as[13]:

$$\Gamma_s = \frac{\sum_{n=1}^{N}(C_n - C_0)}{A(1 - C_0)}$$

where the sum is over all of the atoms under consideration, C_n is the concentration of the nth atom (i.e. 1 if the nth atom is solute s, and 0 otherwise), C_0 is the concentration of solute s in the matrix and A is area of the grain boundary. The Gibbsian excess value varies from dataset to dataset but shows no significant difference between crystal bar Zr and ZrFeCr as shown in **Table 3**. Therefore Fe segregation to the metal grain boundaries alone cannot explain the difference in the oxide stability.

Table 3: Average measured Gibbsian excesses (atom/nm^2). The uncertainty is the standard deviation over the number of analyses indicated in ().The number of grain boundary examined is indicated in <>.

	Crystal bar Zr	ZrCrFe
Zr(O)	3.9 ± 1.9 (5)<3>	2.7 (1) <1>
Zr(O)sat	5.7 ± 1.1 (2)<2>	5.7 (1) <1>

5.5. Summary

The distribution of alloying elements is modified in the oxygen-rich region of the metal next to the oxide front. Segregation and clustering of Fe and Sn are observed along grain boundaries in ZrO_2, at ZrO_2/ZrO and ZrO/$Zr(O)_{sat}$ interfaces. Fe also segregates to linear features, probably dislocations, which mostly run parallel to the ZrO/$Zr(O)_{sat}$ interface. Fe-decorated dislocations are observed only in the $Zr(O)_{sat}$ layer and in the solid solution near the oxide/metal interface while there are absent in the metal substrate away from interface. The presence of dislocations can be rationalized in terms of local strains induced by the growing oxide that is associated with a significant volume change.

Quantitative analysis shows that Fe segregation levels are comparable for both crystal bar Zr and ZrFeCr. Therefore Fe segregation to the metal grain boundaries alone cannot explain the difference in the oxide stability.

6. Early stages of oxidation

At the initial stage of oxidation, the oxide layers on pure Zr and ZrFeCr are about the same thickness (less than 1 um) (**Figure 18**) with some variations in the oxide thickness from grain to grain. The variation of oxide thickness indicates different oxygen diffusion rate along different crystallographic directions, as discussed in following section. Slight ingress of the oxide front along some grain boundaries in pure Zr was also observed in pure Zr but not in Zr-Fe-Cr alloy (**Figure 19**). The slight ingress along grain boundaries in pure Zr further developed into dendrites of oxide penetrating farther into metal grain boundaries after 55 days of oxidation, whereas the oxide/metal interface in ZrFeCr still remains relatively flat.

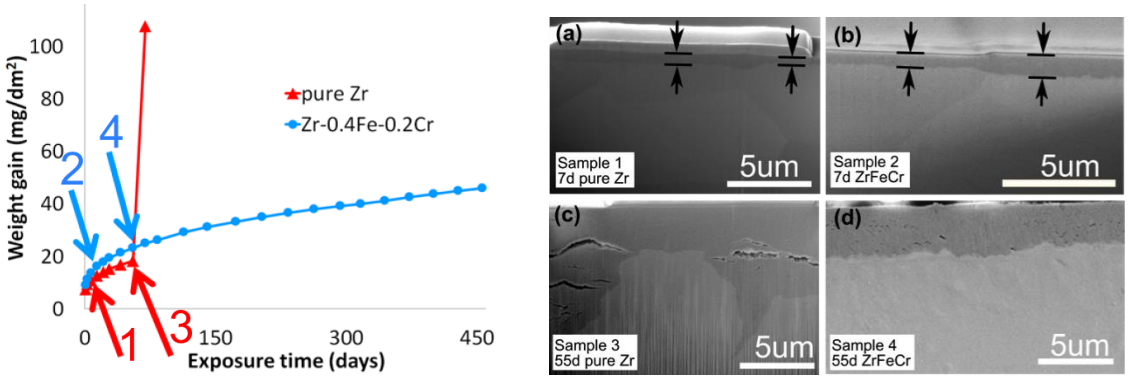

Figure 18: (left) Corrosion weight gain versus exposure time in 360°C pure water for pure Zr and ZrFeCr (right) SEM images of four oxidized Zr samples indicated in the weight gain curves.

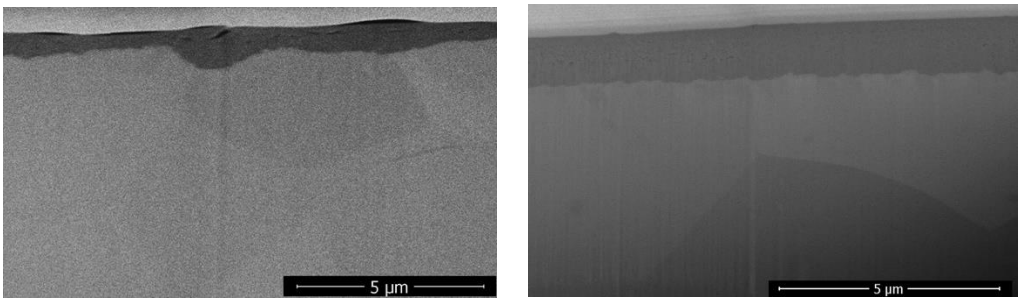

Figure 19: SEM images of (left) 7 days pure Zr sample showing the faster oxide growth along grain boundary; (right) ZrFeCr sample showing no preferential oxidation along grain boundary.

6.1. Initial oxide growth rate and crystallographic orientation of the metal substrate

The correlation between oxide thickness and the orientation of the metal grain beneath was studied by combining FIB cross sectional imaging for measuring the thickness of the oxide layer and orientation mapping to characterize the orientation of the underlying Zr grains as illustrated in **Figure 20**. The orientation dependence of the ZrO_2 oxide thickness for crystal bar Zr, Zircaloy-4, and ZrFeCr were evaluated and shown in **Figure 21**. In crystal bar Zr and Zircaloy-4, the oxide thickness appears to increase when advancing along metal grains in which the basal orientation of the grains is more parallel to the oxide/metal interface, while the growth rate in ZrFeCr appears to be independent of orientation. We note that the oxide measured here is only ZrO_2 as the sub-oxides are not visible in the SEM images.

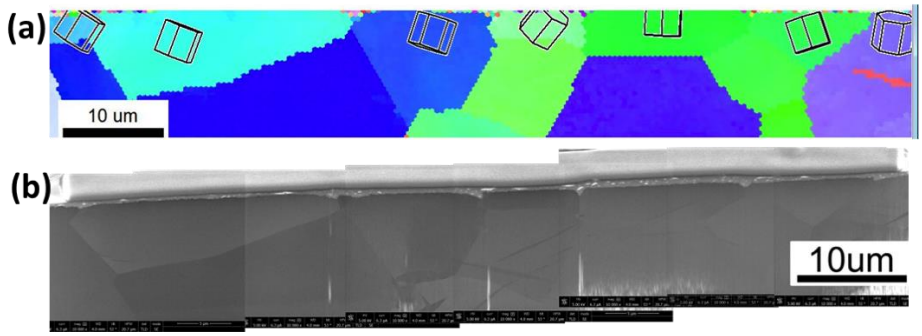

Figure 20: (a) Inverse pole figure (IPF) and (b) stitched SEM image that illustrate the correlation between oxide (ZrO2) thickness and orientation of metal grain beneath.

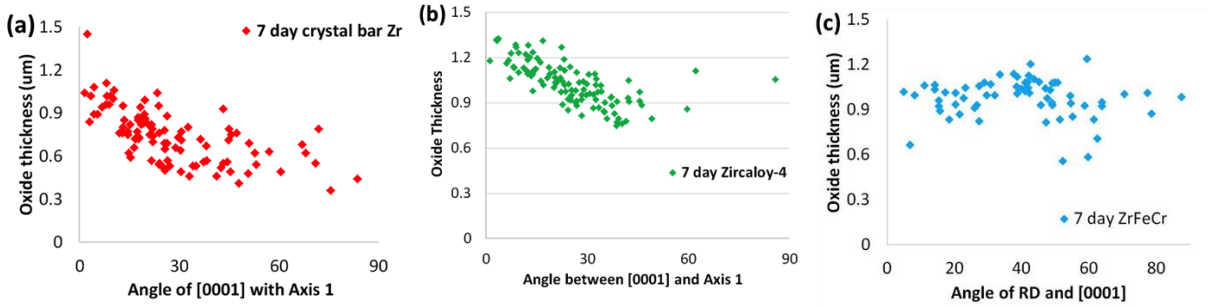

Figure 21: Oxide thickness as a function of grain orientation for crystal bar, Zircaloy-4, and ZrFeCr oxidized for 7 days. Axis 1 represents the normal to the metal surface.

The distribution of misorientation angles for the metal grain boundaries both crystal bar Zr and ZrFeCr are given in **Figure 22**, where no obvious differences can be observed. This means that both the overall texture and the local grain-to-grain misorientation are similar in the two alloys, so that it is unlikely that the texture difference would play a role in the different oxidation behaviors between crystal bar Zr and ZrFeCr. Therefore the mechanism must be linked to chemistry.

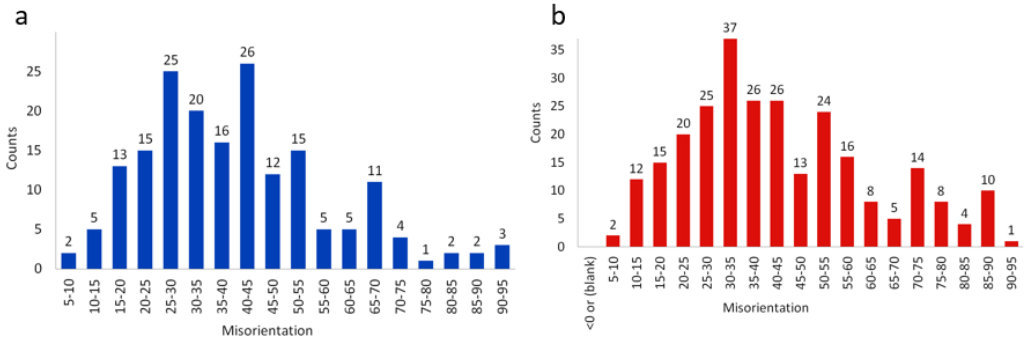

Figure 22: Distribution of grain boundary misorientation angles in (a) crystal bar Zr and (b) ZrFeCr.

The decreasing trend we observed in crystal bar Zr and Zircaloy-4 contradicts prior work[14], where a lower (instead of higher) oxidation rate was observed on zirconium single crystals oriented with the <0001> direction

perpendicular to the oxide/metal interface. This discrepancy has yet to be clarified. The authors also reported a strongly textured oxide film with oxide (002) or (200) planes oriented parallel to the oxide/metal interface regardless of how the metal grains were oriented. Conversely, as described in the coming section, we observed a clear orientation relationship between zirconium metal and the oxide grains. It is possible that in the early stages of oxide growth where strains are not yet significant, the oxide grain orientation distribution is driven by the orientation relationship with the underlying metal. At later stages when the oxide thickness becomes significant, a strong oxide texture may develop driven by strain minimization.

6.2. Oxygen ingress along metal grain boundaries

Different Fe and O distributions along grain boundaries in the metal and oxide phases are observed depending on the grain boundaries and seem to correlate with oxide ingress along grain boundaries. Three different cases are illustrated in **Figure 23**. In dataset A (crystal bar Zr), the oxygen concentration increases at the grain boundary, from ~20% to ~50%, leading to the formation of the ZrO phase. The Fe segregation along the grain boundary extends from the metal into the oxide. From the SEM image, a vertical crack has formed on the top of the oxide layer, pointing at a direction parallel with grain boundary, accompanied by a steep oxide advance at the grain boundary. In dataset B (crystal bar Zr), the Fe segregation visible along the metal grain boundary is interrupted at the oxide/metal interface. This can be interpreted as either the grain boundary does not extend into the oxide phase or that the boundary does extend but is not decorated by Fe. A crack and faster oxide growth along the grain boundary are also observed, but the crack propagation direction is not along the grain boundary plane and there is no steep oxide advance along the grain boundary. In data J (ZrFeCr), neither faster oxide advance along grain boundary nor crack propagation is evident. The difference between the three datasets indicates that the differences in oxide microstructures or chemistry are more likely to contribute to the faster oxidation along metal grain boundaries and oxide growth instabilities.

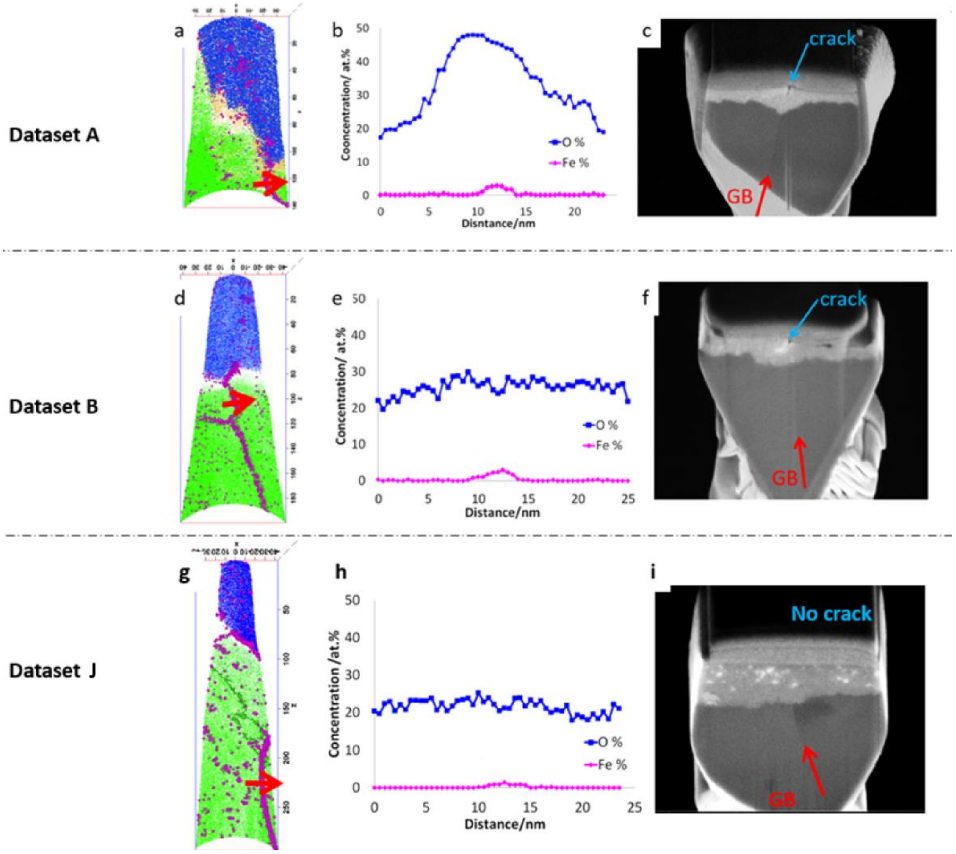

Fig. 23: Three representative APT reconstructions from crystal bar Zr (dataset A and B) and ZrFeCr (dataset J). The Fe and O concentration profiles (b, e, h) were measured by placing a 10nm diameter cylinder along the

arrows in the respective dataset (a, d, g). The SEM images (c, f, i) of non-sharpened APT tips show the grain boundaries and different cracking behaviors near grain boundaries region.

6.3. Initial observations on the structure of the ZrO_2 scale

The oxide microstructures at initial stage of oxidation were studied by transmission electron microscopy (TEM) and the results are summarized in **Figure 24**. We tilted the metal grains with its [-12-10] zone axis parallel to electron beam and recorded the electron diffraction patterns of both metal grain and oxide layers. An interesting finding is that, even though the oxide layer consists of large numbers of nano-sized grains, the majority of the grains share very similar orientation, producing a spot diffraction pattern. By superimposing the oxide diffraction patterns onto the respective metal grains diffraction patterns, we are able to demonstrate that there is an orientation relationship between zirconium metal and oxide grains. Similar electron diffraction analysis on ZrFeCr alloy exhibits patterns more like ring patterns with a weaker texture than in crystal bar Zr (**Figure 25**).

There have been many attempts to determine the orientation relationship between zirconium metal and zirconium oxide. Some work concluded that there was no specific orientation relationship between α-Zr and monoclinic ZrO_2[14]. Instead, the oxide grains grow along the <001> direction and align their (002) planes parallel to the oxide/metal interface in order to minimize compressive stresses. However, more recent work using electron diffraction pattern and HRTEM suggested that the (10-10) plane of α-Zr are parallel to the (111)[15], (200) or (020)[8] plane of ZrO_2. Based on our findings, there were no planes in ZrO_2 that perfectly aligned with (10-10) plane of α-Zr. However the angle between one set of plane (likely (111)) with the (10-10) plane of α-Zr is very small (~5°).

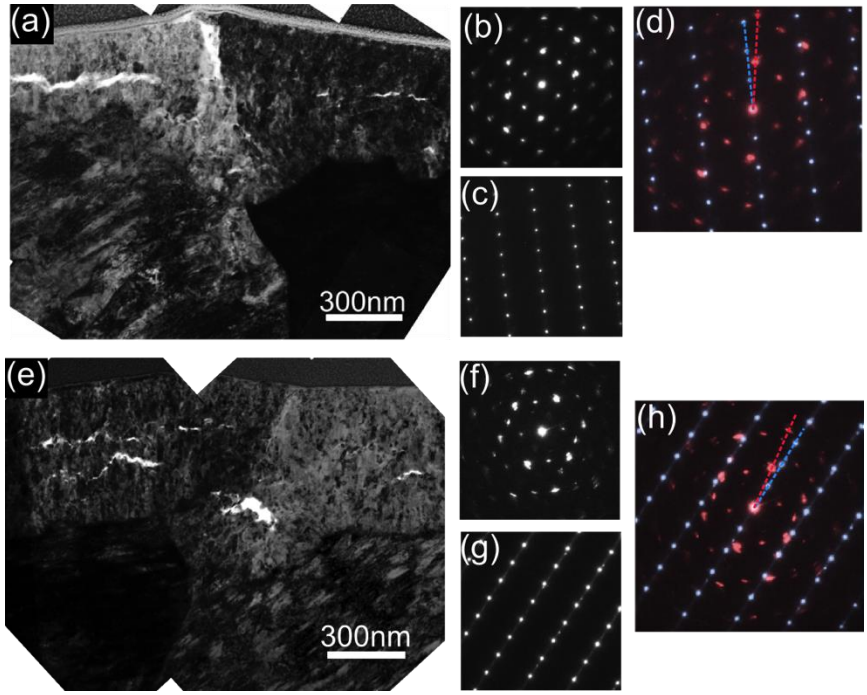

Figure 24: TEM bright field images (a) of lift-out samples that taken from grain boundary in 1 day crystal bar Zr. (b) and (e) electron diffraction patterns taken from oxide layers when the metal grains were tilted to [-12-10] zone axis as shown in (c) and (g). Diffraction patterns from metal and oxide were superimposed in (d) and (h), where orientation relationship between the metal and oxide was the same for both samples.

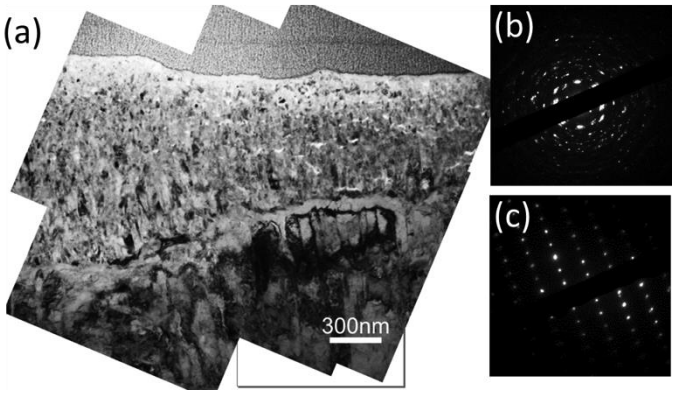

Figure 25: (a) TEM bright field image of 7 day ZrFeCr; (b) electron diffraction pattern taken from oxide layers when the metal grains were tilted to [-12-10] zone axis as shown in (c).

6.4. Summary

We observed an increase in the ZrO_2 oxide thickness as the basal plane of the grains is more parallel to the oxide/metal interface in crystal bar Zr and Zircaloy-4 while the growth rate in ZrFeCr appears to be independent of orientation. Even though the grain structure of the ZrO_2 scale is nano-crystalline, a very strong oxide texture is found on crystal bar Zr compared to the oxide forming on ZrFeCr. The texture is rationalized in terms of a preferred crystallographic orientation between Zr and ZrO_2.

We hypothesize that interfacial chemistry may play a role on the orientation selection of the new grains nucleating at the Zr or suboxide / ZrO_2 interface.

A great degree of preferential orientation in the oxide layer can contribute to significant amount of stress building up in that layer and in the underlying metal substrate. This may promote cracking and also promote faster oxide growth along metal grain boundaries. In fact, cracks and faster oxide advance along grain boundary seems to correlate with a continuous Fe segregation that extends from metal to oxide. We also hypothesize that differences in the structure and chemistry of the oxide scales are more likely to contribute to the faster oxidation along metal grain boundaries and oxide growth instabilities than the underlying metal microstructure.

7. Conclusions

In this project, we have used a multi-scaled characterization approach to study the oxidation behavior of zirconium alloys and determine the origins of the wide range of behaviors. We conducted a detailed analysis of the microstructures and chemistry of oxide and suboxide phases, metal/oxide interface, and bulk metal in alloy samples that have different compositions and different corrosion time. The findings are summarized as follows:

- A consistent sequence of sub-oxide phases is observed ahead of the ZrO_2 oxide front, consisting of (i) a thin layer of equiatomic ZrO (occasionally slightly over and under stoichiometric but variation might come from evaporation artifact) (ii) saturated solid solution $Zr(O)_{sat}$ with a constant oxygen concentration consistent with the Zr_2O stoichiometry, and (iii) a slowly decreasing oxygen profile into the metal.
- The width of intermediate oxide layers depends both on the alloy and on the stage of corrosion. In general, the thicknesses of the suboxide phases are inversely correlated to the oxidation rate.
- The distribution of alloying elements is modified in the oxygen-rich region of the metal next to the oxide front. Segregation and clustering of Fe and Sn are observed along grain boundaries in ZrO_2, at ZrO_2/ZrO and ZrO/$Zr(O)_{sat}$ interfaces.
- Fast oxide growth and formation of oxide dendrites along the grain boundary were observed in crystal bar Zr. Fe segregations on grain boundaries in the metal are not likely to be the reason for dendrites formation.
- Clear dependency of oxide grain orientation on the metal grain is observed in crystal bar Zr but not as significant in ZrFeCr, which might cause the stress built-up and crack formation in the oxide layer near grain boundary regions.

However, further work is required to link the effect of oxide microstructures on the faster oxide growth along grain boundaries. This work clearly showed that chemistry of the base metal alone cannot explain the observed oxidation behaviors. The synergy between oxide chemistry (segregation at grain boundaries and oxide interfaces) and oxide texture is also playing a role in promoting fast oxide growth along the grain boundary in crystal bar Zr or stabilizing the ZrO_2 film in ZrFeCr, a role that is yet to be determined.

8. Acknowledgments

This work was supported by the University of Michigan College of Engineering (Access and User of the characterization equipment at the Michigan Center for Materials Characterization), DOE Office of Nuclear Energy's Nuclear Energy University Programs at the University of Michigan and University of California-Santa Barbara Colleges of Engineering, and the ATR-NSUF program (carrying out the UCSB ATR-1 irradiation and handing and preparation of active specimens).

1. Presentations and Publications

Presentations

1. International Symposium on Plasticity, Keynote Speaker in Symposium Dedicated to Bill Nix, Puerto Vallarta, MX, January 2011: "Understanding the Role of Twin Boundaries in Radiation Damage of Stainless Steels"
2. 2011 Science on Saturday Lecture Series, Princeton University, Princeton, NJ, January 2011: "Electrons, Camera, Action: Dynamic Electron Microscopy to Understand Materials for Energy"
3. Alcoa Technical Center, Alcoa Center, PA, February 2011: "Multiscale Microscopy for Predictive Alloy Development"
4. Penn State, Department of Materials Science & Engineering, State College, PA, March 2011: "Dynamic TEM for the Study of Interfacial Mechanisms in Materials
5. Agilent Symposium, "In Situ TEM Techniques: Spanning Time and Length Scales," Winter 2010
6. Pennergy Center Symposium on Materials in Extreme Environments, University of Pennsylvania, Philadelphia, PA, April 2011: "In Situ and Ultrafast TEM Techniques for Understanding Materials Behavior in Extreme Environments"
7. Argonne Users Week, Argonne National Laboratory, Argonne, IL, May 2011: "Direct Observation of Microstructural Effects on Domain Switching in Multiferroic Oxides"
8. Carpenter Technology, Reading, PA, May 2011: "Manipulating Grain Boundary Population for Improved Properties in Stainless Steels"
9. Idaho National Laboratory User Week, Idaho Falls, ID, June 2011: "Electron Microscopy Techniques for Understanding Radiation Damage"
10. ISAF-PFM International Meeting on Ferroelectric and Polar Materials, Vancouver, BC, July 2011: "Direct Observation of Defect-Domain Interactions in BFO Using In Situ TEM"
11. Oxides Fest Conference at Drexel, Philadelphia, PA, August 2011: "Dynamic Characterization Group: Dynamics of Defect Interactions in Oxides"
12. University of Delaware, Department of Materials Science & Engineering, Newark, DE, September 2011: "In situ TEM Across Multiple Time and Length Scales"
13. Holtec International, Cherry Hill, NJ, October 2011: "Toward Corrosion Resistant Materials for Nuclear Waste Storage"
14. International Symposium on Plasticity, San Juan, Puerto Rico, January 2012: "Grain Boundary Dependent Radiation Damage"
15. Sandia National Laboratory Colloquium, Albuquerque, NM, February 2012: "Approaches to Radiation Tolerance Through Interfacial Engineering"
16. TMS Annual Meeting, Orlando, FL, March 2012: "In Situ Studies of Domain Switching in Ferroelectrics"
17. Pacific Northwest National Laboratory, Richland, WA, March 2012: "Multiscale In-Situ Studies of Microstructural Evolution in Extreme Environments: Challenges and Opportunities"
18. Electric Power Research Institute, Charlotte, NC, May 2012: "Multi-scale Investigation of the Influence of Grain Boundary Character on RIS and Mechanical Behavior in LWR Steels"
19. Argonne National Laboratory Annual APS/CNM/EMC Meeting, Argonne, IL, May 2012: "Application of In Situ TEM Methods to "Real" Devices and Structures: Challenges and Opportunities"
20. NC State University, Raleigh, NC, October 2012: "Quantitative Analysis of Interfacial Phenomena Using In Situ TEM Techniques"
21. MS&T Annual Meeting, Pittsburgh, PA, Fall 2012: "Predictive Microstructural Evolution Studies: Correlation of Orientation Imaging with In Situ TEM"
22. ASM Young Members Night, Liberty Bell Chapter, Philadelphia, PA, November 2012: "Engineering Microstructures for Radiation Tolerance in Nuclear Materials"
23. CAARI 2012 (22nd International Conference on the Application of Accelerators in Research and Industry), Dallas, TX, August 2012: "In-Situ TEM Observation of the Grain Size Effect on Radiation Induced Defect Distribution in Iron"
24. International Symposium on Plasticity, Nassau, Bahamas, January 2013: "Grain Boundary Character and Density Effects on Radiation Damage in Nanocrystalline Metals"
25. International Symposium on Plasticity, Nassau, Bahamas, January 2013: "Predictive Microstructural Evolution Studies: Correlation of Orientation Imaging with In Situ TEM"
26. Idaho National Laboratory, Idaho Falls, ID, January 2013, "Predictive Understanding of Radiation Damage and Corrosion Using In Situ TEM Techniques""
27. M. Taheri, "In Situ Characterization of Interfaces in Reactor Environments," Workshop on Nanomaterials & Engineered Microstructures for Nuclear Applications (NEMNA), Brookhaven National Laboratory, March 2013

28. E. Marquis, "Atom Probe Tomography of Oxides in Zr-based Alloys," Workshop on Nanomaterials & Engineered Microstructures for Nuclear Applications (NEMNA), Brookhaven National Laboratory, March 2013
29. University of Virginia, Department of Materials Science & Engineering, Charlottesville, VA, April 2013: "Predictive Understanding of Material Behavior in Extreme Environments Using In Situ TEM Techniques"
30. 4th International Workshop on Remote Electron Microscopy and In situ Studies, Lisbon, Portugal, May 2013: "Predictive Microstructural Evolution Studies: Correlation of Orientation Imaging with In Situ TEM"
31. International Workshop on Advancing Materials Performance from the Nanoscale, Xi'an Jiaotong University, Xi'an, China, June 2013: "Predictive Microstructural Evolution in Extreme Environments Using In Situ TEM Techniques"
32. National Center for Electron Microscopy, Tsinghua University, Beijing, China, June 2013: "In situ TEM Techniques For Analysis of Interfacial Dynamics in Oxides and Metals"
33. Shanghai Jiaotong University, Shanghai, China, June 2013: "Correlation of Orientation Imaging and In situ TEM in Extreme Environments"
34. Shanghai Advanced Research Center, Chinese Academy of Sciences, Shanghai, China, June 2013: "Predictive Microstructural Evolution in Extreme Environments Using In Situ TEM Techniques: Opportunities and Challenges"
35. Idaho National Laboratory Users Week, June 2013: "Overview of Drexel Advanced Test Reactor Program: Grain Boundary Dependency of Radiation Induced Segregation"
36. E.A. Marquis, *Atomic scale chemistry of interfaces,* **Los Alamos National Laboratory**, July 2013
37. Center for Defect Physics, Oak Ridge National Laboratory, Oak Ridge, TN, September 2013: "Understanding Radiation Induced Defect Migration Mechanisms in Nanocrystalline Fe using In Situ TEM Techniques"
38. 2014 PM World Congress Program Committee Meeting, "Electrons, Camera, Action: Advanced In Situ and High Resolution Microscopy Techniques for Understanding Microstructure-Property Relationships in Alloys"
39. MS&T 2013, Montreal, QC, October 2013: "Observing Strain Dependence of Twin Boundary Formation Using Correlated Precession Diffraction and In Situ TEM"
40. MRS, Fall 2013, Boston, MA, December 2013: "Nanostructured Materials under Ion Irradiation in situ the IVEM-Tandem Facility at ANL"
41. TMS Annual Meeting 2014, San Diego, CA, February 2014: "Analysis of Localized Strain Dependencies during Microstructural Evolution by Correlated Precession Diffraction and In Situ TEM"
42. TMS Annual Meeting 2014, San Diego, CA, February 2014: "Insight into Microstructural Evolution during Severe Plastic Deformation Processes Gained from In Situ Microscopy"
43. TMS Annual Meeting 2014, San Diego, CA, February 2014: "Grain Boundary-defect Interactions Under Loading of Irradiated Nanocrystalline Films"
44. (Invited) E.A. Marquis, Y. Dong, A. Motta, *Insights into Atomic Scale Microstructures of Zr Alloys under Corrosive Environments*, Annual TMS meeting, San Diego, CA (Feb 2014)
45. Johns Hopkins University, March 2014: "Quantitative Analysis of Interfacial Phenomena Using In Situ TEM Techniques"
46. General Motors, Warren, MI, March 2014: "Electrons, Camera, Action: Advanced In Situ Microscopy Techniques for Understanding Microstructural Evolution in Metals"
47. W. Harlow, H. Ghassemi, M. Taheri "In-situ TEM Study of the Corrosion Behavior of Zry-4," Microscopy and Microanalysis annual meeting, August 2014
48. Department of Energy NE-SC Information Exchange Meeting, September 2014: Washington, D.C., "Issues and Opportunities for Next Generation Nuclear Reactor Materials"
49. Society of Engineering Science (SES) 51st Annual Technical Meeting, Microscale and Microstructural Effects on Mechanical Behavior Symposium, West Lafayette, IN, October 2014: "Predictive Microstructural Evolution via Localized Strain Dependence Measurements Using Correlated Precession Diffraction and In Situ TEM"
50. W. Harlow, H. Ghassemi, M. Taheri "Phase Identification in Early Stages of Corrosion in Zircaly-4," 2014 MRS Fall Meeting & Exhibit, December 2014
51. 21st International Symposium, Plasticity, Damage and Fracture, Plasticity and Microstructural Evolution in Nanostructured Materials Symposium, Montego Bay, Jamaica, January 2015: "Measurement of Geometrically Necessary Dislocation Content Using Precession Electron Diffraction"

52. TMS Annual Meeting, Orlando, FL, March 2015: "Al-Mg Alloy Sensitization and Failure in Marine Environments"
53. Purdue University, Departments of Materials Science & Engineering and Aeronautics and Aerospace Engineering, March 2015: "Coupling Quantitative Strain Measurement with In Situ TEM"
54. Y. Dong, A. Motta, E.A. Marquis, Solute Distributions in Oxide and Sub-Oxide Layers during Corrosion of Zirconium Alloys, Annual TMS meeting, Orlando, FL (March 2015)
55. W. Harlow, H. Ghassemi, M. Taheri "Early Stage Corrosion Study of Zircaloy-4 Inside A Transmission Electron Microscope," Annual TMS meeting, Orlando, FL (March 2015)
56. Hopkins Extreme Materials Institute (ARL CRA) MACH Conference, In-situ, Time-resolved Measurements and Computational Modeling Symposium, Annapolis, MD, April 2015: "Predictive Microstructural Evolution via Localized Strain Dependence Measurements Using Correlated Precession Diffraction and In Situ TEM"
57. Cameca Atom Probe Users Meeting, Madison, Wisconsin, June 2015, "Correlating APT and TEM for High Resolution Chemical Analysis of Interfaces"
58. Carpenter Technology, June 2015, Understanding Radiation Damage at the Nanoscale: Dislocation-Grain Boundary Interactions
59. Microscopy and Microanalysis Annual Meeting, Portland, OR, August 2015: "The Perfect Cut: Focused Ion Beam Preparation for In Situ TEM"
60. Microscopy and Microanalysis Annual Meeting, Portland, OR, August 2015: "Toward Deterministic Switching in Ferroelectric Systems: Insight Gained from In Situ TEM"
61. PoliFab Center, Politecnico di Milano, August 2015, "Predictive Microstructural Evolution via Localized Strain Dependence Measurements Using Correlated Precession Diffraction and In Situ TEM"
62. W. Harlow, M. Taheri "In-situ TEM Study of the Initial Oxidation Behavior of Zry-4," Microscopy and Microanalysis annual meeting, August 2015
63. Oak Ridge National Laboratory CNMS Workshop, September 2015, "Current State of In Situ TEM for Electronic Device Analysis"
64. NYU-Poly Department of Mechanical Engineering, October 2015, "Predictive Microstructural Evolution via Localized Strain Dependence Measurements Using Correlated Precession Diffraction and In Situ TEM"
65. Villanova University Department of Mechanical Engineering, October 2015, "Predictive Microstructural Evolution via Localized Strain Dependence Measurements Using Correlated Precession Diffraction and In Situ TEM"
66. MS&T, October 2015, Columbus, Ohio, "Predictive Microstructural Evolution via Localized Strain Dependence Measurements Using Correlated Precession Diffraction and In Situ TEM"
67. MRS fall 2015, Boston, MA, "Toward Deterministic Switching: Quantitative In Situ TEM Studies of Ferroelectric Domain Behavior"
68. W. Harlow, M. Taheri, "In-situ TEM of the First Stages of Oxidation," Materials Science and Technology 2015, October 2015
69. Plasticity 2016, Kona, Hawaii, Understanding Radiation Damage at the Nanoscale: Dislocation-Grain Boundary Interactions
70. MRS spring 2016, Phoenix, Arizona, Probing the "Immunity" of Grain Boundaries under In Situ Irradiation in Nanocrystalline Metals
71. Thermec 2016- Graz, Austria, "Predictive Microstructural Evolution via Localized Strain Dependence Measurements Using Correlated Precession Diffraction and In Situ TEM"

Publications

1. On the current role of atom probe tomography in materials characterization and materials science, EA Marquis, M Bachhav, Y Chen, Y Dong, L Gordon, A McFarland, **Current Opinion in Solid State and Materials Science** (2013) accepted
2. Atom Probe Tomography Study of Alloying Element Distributions in Zr Alloys and their Oxides, Y Dong, A Motta, EA Marquis, **Journal of Nuclear Materials** (2013) 442(1-3) 270-281
3. In Situ Environmental Transmission Electron Microscopy Study of the Oxidation of Two-Dimensional Ti3C2 and Formation of Carbon-Supported TiO2, H. Ghassemi, W. Harlow, O. Mashtalir, M. Beidaghi, M. Lukatskaya, Y. Gogotsi, M.L. Taheri, **Journal of Materials Chemistry A** (2014) accepted

4. EELS and Atom Probe Tomography study of the evolution of the metal/oxide interface during zirconium alloy oxidation, B de Gabory, Y Dong, A Motta, EA Marquis **Journal of Nuclear Materials** (2015) 462 304-309
5. Determination of the Initial Oxidation Behavior of Zircaloy-4 by *In-Situ* TEM, W. Harlow, H. Ghassemi, M. L. Taheri, **Journal of Nuclear Materials** (2016) 474 126-133
6. Stress-stabilization of Tetragonal ZrO_2 as a Function of TEM Sample Thickness, W. Harlow, M.L. Taheri, In Preparation
7. Oxide Nucleation Location and Initial Phase in Zirconium as Determined Using In-Situ TEM, W. Harlow, M.L. Taheri, In Preparation

5. References

1. DOE-NERAC (2002). A Technology Roadmap for Generation IV Nuclear Energy Systems, GIF-002-00**.**
2. Allard, L.F. (2009) Bigelow, W.C. Jose-Yacaman, M., Nackashi, D.P. Damiano, Mick SE. "A new MEMS-based system for ultra-high-resolution imaging at elevated temperatures," Microscopy
3. Research and Technique (Special Issue: In Situ Electron Microscopy Methods) Volume 72, Issue 3, pages 208–215, March 2009
4. Allen, T. (2004). "Evaluation of Candidate Materials for Supercritical Water Cooled Reactors". 4th SCWR Information Exchange Meeting, Pittsburgh.
5. Allen, T. R. and D. C. Crawford (2003). "Fuels and Materials Needs for Generation IV Nuclear Energy Systems". Proceedings of the ICAPP'03, Spain, American Nuclear Society. **Paper no. 3237**.
6. Bischoff, J. B., A. T. Motta, et al. (2009). "Evolution of the Oxide Structure of 9CrODS Exposed to Supercritical Water " Journal of Nuclear Materials **392**: 272–279.
7. Hauffe, K. (1965). "Oxidation of Metals". New York, Plenum Press.
8. Hudson, D., Cerezo, A. et al. (2009a). "Zirconium oxidation on the atomic scale." Ultramicroscopy **109**(5): 667-671.
9. Hudson, D. and Smith, G.D.W. (2009b). "Initial observation of grain boundary solute segregation in a zirconium alloy (ZIRLO) by three-dimensional atom probe." Scripta Materialia **61**(4): 411-414.
10. IAEA (1993). Corrosion of Zirconium Alloys in Nuclear Power Plants. IAEA-TECDOC-684**.**
11. IAEA (1998). Waterside Corrosion of Zirconium Alloys in Nuclear Power Plants, IAEA-TECDOC-996**.**
12. Kunkle, J., A. T. Motta, et al. (2008). "Characterization of HT-9 ferritic-martensitic steels oxidized in lead bismuth eutectic", Anaheim, CA, Transaction of the American Nuclear Society. **98:** 1115-1116.
13. Lozano-Perez, S; Saxey, D W; Yamada, T; Terachi, T. Atom-probe tomography characterization of the oxidation of stainless steel Scripta Mater. , 62(11): 855-858 201
14. Marquis, E.A., Hyde, J.M. et al. (2009). "Nuclear reactor materials at the atomic scale." Materials Today **12**(11): 30-37.
15. Marquis, E.A., Yahya, N.A. et al. (2010). "Probing the improbable: imaging carbon atoms in alumina." Materials Today **13**: 42.
16. Motta, A., A. Yilmazbayhan, et al. (2007). "Zirconium Alloys for Supercritical Water Reactor Applications: Challenges and Possibilities." Journal of Nuclear Materials **371**: 61-75.
17. N. de Jonge, D. B. Peckys, G.J. Kremers and D.W. Piston (2009a), "Electron microscopy of whole cells in liquid with nanometer resolution", *PNAS*, vol. 106, pp. 2159-2164, 2009.
18. N. de Jonge, M.J. Dukes, G.J. Kremers, B.M. Northan, D.B. Peckys, E.A. Ring, DW Piston and R Sougrat, (2009b) "Liquid and Three-Dimensional Scanning Transmission Electron Microscopy for Biological Specimens", *Microscopy and Microanalysis*, vol. 15, pp. 686-687, 2009.
19. N. de Jonge, N. Poirier-Demers, H. Demers, D.B. Peckys, and D. Drouin, (2010) "Nanometer-resolution electron microscopy through micrometers-thick water layers", *Ultramicroscopy*, vol. 110, pp. 1114-1119, 2010.
20. Saxey, D.W., Cairney, J.M. et al. (2007). "Atom probe specimen fabrication methods using a dual FIB/SEM." Ultramicroscopy **107**: 756
21. Tan, L., K. Sridharan, et al. (2008). "Altering corrosion response via grain boundary engineering." Materials Science Forum **595**-**598**: 409-18.
22. Thompson, K., Lawrence, D. et al. (2007). "In situ site-specific specimen preparation for atom probe tomography." Ultramicroscopy **107**(2-3): 131-139.

23. Yang, R., O. Ozer, et al. (2000). "Current Challenges and Expectations of High Performance Fuel for the Millenium". Light Water Reactor Fuel Performance Meeting, Park City, Utah, ANS.
24. B. Hutchinson, B. Lehtinen, M. Limbach, and M. Dahlback, "A study of the structure and chemistry in zircaloy-2 and the resulting oxide after high temperature corrosion," Sunriver, OR, United states, American Society for Testing and Materials, 1505 STP, (2009), 269-284.
25. A. Yilmazbayhan, A. T. Motta, R. J. Comstock, G. P. Sabol, B. Lai, and Z. Cai, "Structure of Zirconium Alloy Oxides formed in pure water studied with Synchrotron radiation and optical microscopy: relation to corrosion rate," *Journal of Nuclear Materials* 324 (2004) 6-22.
26. A. Yilmazbayhan, E. Breval, A. Motta, and R. Comstock, "Transmission Electron Microscopy Examination of Oxide Layers Formed in Zr Alloys," *Journal of Nuclear Materials* 349 (2006) 265-281.

5. Milestone Status

Year	Task	Milestone	Completion date/Deliverable	Actual Completion date	Percent Completed
1	1	Task A1: Design and fabrication of in situ environmental TEM holder	Personnel hired; ample preparation process completed; holder design process complete; holder being built, to be delivered in December 2012.	Design complete; first fabrication complete by 12/31/2012	100%
1	2	Task B1: Sample selection and initial grain boundary analysis in 3 Zr alloys (both bare alloys and oxidized alloys) by APT. Parallel TEM examinations to be conducted.	Sample selection complete; student hiring and training complete; GB analysis ongoing.	GB analysis in bulk alloys will be completed by 1/31/2012	95%
2	1	Task A1: Design and fabrication of in situ environmental TEM holder	Stage delivered to Drexel in Phase 1 format	Phase 1 analysis began; Phase 2 to be implemented later quarters.	100%
2	1	Task B1: Sample selection and initial grain boundary analysis in 3 Zr alloys (both bare alloys and oxidized alloys) by APT. Parallel TEM examinations to be conducted.	Atom Probe and TEM work beginning to converge. Preliminary work completed.	In situ work on specific GBs to be compared to atom probe in next quarter.	75%
2	2	Task B2: Establish evolution of oxide/metal interface and GB chemistry at various oxidation stages in 3 different Zr alloys. Correlate to corrosion kinetics	Calibration of Atom Probe and TEM for correlative studies completed	Work on mechanisms next quarter	35%
2	3	Task B3: Select samples and grain boundary types to be examined in situ	Select GB types for initial in situ experiments	Initial work on pure Zr samples being performed	35%

3	1	Task A2: Perform in situ corrosion on Zr alloy samples and grain boundary types selected previously.	Initial in situ corrosion tests completed. In-situ parameters being refined	In situ work on specific GBs next quarter	45%
3	3	Task B3: Analysis and integration of in situ results and examinations of bulk samples. Select F-M samples for in situ corrosion	Comparison of bulk samples to in-situ samples. Selection of in situ F-M steel samples	Initial comparison of bulk samples to in situ results has been completed	15%
4	3	Task A3: Create APT samples from F-M and Zr alloys exposed in situ to compare grain boundary chemistry to bulk samples	Comparison of GBs in bulk and in situ samples	Initial in situ samples shipped to UM for evaluation of technique	1%

2. Budget Data

			Approved Spending Plan		Actual Spending	
	From	To	Quarter	Cumulative	Quarter	Cumulative
Yr1: Q1	N/A*	N/A*	N/A*	N/A*	N/A*	N/A*
Yr1: Q2	1/1/2012	3/30/2012	N/A*	N/A*	154,000 encumbered from in situ stage design thus far	154,000 Encumbered
Yr1: Q3	4/1/2012	6/30/2012	3		Drexel: Personnel- **$14,783.65** ($11,182.79(extra research compensation) + $3,600.86(fringe)) Personnel- **$14,783.65** ($11,182.79(extra research compensation) + $3,600.86(fringe)) General: Equipment- $77,275 (spent) and $77,670(encumbered) CRF Charges- $2,050 Printing- $54.00 Indirect- $9,983.45 Total- **$89,362.45** Subcontract all has been encumbered- $585,442 but only $1,430.60(actually paid out). U.Mich: $3,588.89	(same)
Yr. 1 Qtr. 4					**Total** $78,884.75 **Personnel** $32,013.99 **General** $0.00 **Equipment** $ 77,670.00 **Subcontracts** $19,044.10 **Indirect** $27,826.66	Encumbered not spent
Yr 2 Q1					**Personnel-** Post-doc $31,268.70 Graduate $5,670 Fringe $10,162.32 Total- $47,101.02 **General-** Lab Supplies $684.02 Travel $1,435.75 ($450.60(travel) +$985.15(registration)) CRF $6,570.42 Equipment $10,139.08(EA Fischione and Pfeiffer Vacuum, Inc.)/ $77,6700(encumbered on 7/1/2012) Total- $18,829.27 **Direct Cost-** $65,930.29 **Indirect Cost-** $37,267.42 **Total Spent- $103,197.71** Subcontracts: $35,404.73 ($12,138.79 +$23,265.94)	

Yr2: Q2					**Personnel-** Graduate $5,670.00 Total- $5,670.00 **General-** Lab Supplies $4,382.62 Travel $397.00 (travel) CRF $6,570.42 Equipment $77,670.00 Total- $82,449.62 **Direct Cost-** $65,930.29 **Indirect Cost-** $5,695.05 **Total Spent- $117,179.26** Subcontracts: $23,364.59 (University of Michigan only)	
Yr2: Q3					**Personnel-** Graduate $5,670.00 Total- $5,670.00 **General-** Lab Supplies $273.93 Travel $0 Equipment $0 Total- $273.93 **Direct Cost-** $43,486.68 **Indirect Cost-** $3,239.44 **Total Spent- $46,726.12** **Subcontracts:** $112,165.08 **(University of Michigan) and** $24,901.42 **Penn State University)**	
Yr2: Q4					**Personnel-** Graduate $5,670.00 Total- $5,670.00 **General-** Lab Supplies $455.22 Travel $0 Tuition Remission $1,365.00 Equipment $0 Total- $1,820.22 **Direct Cost-** $7,490.22 **Indirect Cost-** $12,099.17 **Total Spent- $27,079.61** **Subcontracts:** $4,204.66 **(University of Michigan) and** $16,075.07 **(Penn State University)** **Total Including Subcontract- $47,359.34**	

Yr3: Q1					**Personnel-** Graduate $6,600.00 Total- $6,600.00 **General-** Lab Supplies $0 Travel $474.61 Tuition Remission $1,365.00 Equipment $0 Total- $1,839.61 **Direct Cost-** $8,439.61 **Indirect Cost-** $3,855.66 **Total Spent- $12,295.27** **Subcontracts:** $0 **(University of Michigan) and** $0 **(Penn State University)** **Total Including Subcontract- $12,295.27**	
Yr3: Q2					**Personnel-** Graduate $9,825.00 Total- $9,825.00 **General-** Lab Supplies $1,483.77 Travel $1,475.00 Tuition Remission $1,365.00 Equipment $1,800.00 Total- $6123.77 **Direct Cost-** $15,948.77 **Indirect Cost-** $8,663.33 **Total Spent- $24,612.10** **Subcontracts:** $22,621.67 **(University of Michigan) and** $36,875.93 **(Penn State University)** **Total Including Subcontract- $84,109.70**	
Yr3: Q3					**Personnel-** Graduate $9,825.00 Total- $9,825.00 **General-** Lab Supplies $104.17 Travel $1,384.50 Tuition Remission $1,365.00 Equipment $2,800.00 Total- $5,653.67 **Direct Cost-** $15,478.67 **Indirect Cost-** $7,691.98 **Total Spent- $23,170.65** **Subcontracts:** $9,332.60 **(University of Michigan) and** $792.68 **(Penn State University)** **Total Including Subcontract- $33,295.93**	

Yr3: Q4					**Personnel-** Graduate $6,600.00 Total- $6,600.00 **General-** Lab Supplies $0 Travel $1,009.05 Tuition Remission $0 Equipment $0 Instructional Media $48.00 Total- $1,057.05 **Direct Cost-** $7,657.05 **Indirect Cost-** $4,173.09 **Total Spent- $11,830.14** **Subcontracts: $3,322.71 (University of Michigan)** **Total Including Subcontract- $15,152.85**	
Yr4: Q1					**Personnel-** Graduate $6,600.00 **Total- $6,600.00** **General-** Lab Supplies $1,461.66 Travel $2,076.60 CRF Fees $2,500.00 Tuition Remission $1,403.00 Business Meals $126.93 Equipment $0 Instructional Media $41.42 **Total- $14,209.61** **Direct Costs-** $14,209.61 **Indirect Costs-** $6,979.59 **Total Spent- $21,189.20** **Subcontracts: $42,407.59 (University of Michigan)** **Total Including Subcontracts- $63,596.79**	
Yr4: Q2					**Personnel-** Graduate $6,600.00 **Total- $6,600.00** **General-** Lab Supplies $40.00 Travel $3,161.16 Tuition Remission $1,403.00 Equipment $0 Instructional Media $38.50 **Total- $4,642.66** **Direct Costs-** $11,242.66 **Indirect Costs-** $5,362.61 **Total Spent- $16,605.27** **Subcontracts: $10,523.21**	

					(University of Michigan) **Total Including Subcontracts- $27,128.48**	

Yr4: Q3					**Personnel-** Graduate $6,600.00 **Total- $6,600.00** **General-** Lab Supplies $31.67 Travel $100.00 CRF Fees $4,300.00 Tuition Remission $1,403.00 Equipment $0 Instructional Media $0 **Total- $12,434.67** **Direct Costs-** $12,434.67 **Indirect Costs-** $5,957.76 **Total Spent- $18,392.43** **Subcontracts: $114,844.82** **(University of Michigan)** **Total Including Subcontracts- $133,237.25**	
Yr4: Q4					**Personnel-** Graduate $6,800.01 **Total- $6,800.01** **General-** Lab Supplies $1,451.55 Travel $1,578.11 CRF Fees $4,300.00 Tuition Remission $0 Equipment $0 Instructional Media $40 **Total- $14,169.67** **Direct Costs-** $14,169.67 **Indirect Costs-** $7,504.48 **Total Spent- $21,674.15** **Subcontracts: $8,912.04** **(University of Michigan)** **Total Including Subcontracts- $30,586.19**	
Yr5: Q1					**Personnel-** Graduate $8,800.00 **Total- $8,800.00** **General-** Lab Supplies $0 Travel $950.52 CRF Fees $0 Tuition Remission $2,874.00 Equipment $0	

					Instructional Media $0 **Total- $3,824.52** **Direct Costs-** $10,893.27 **Indirect Costs-** $7,370.85 **Total Spent- $18,264.12** **Subcontracts: $88,662.96** **(University of Michigan)** **Total Including Subcontracts- $109,658.33**	